


Prediction of the Properties of the Rare-Earth Magnets $\text{Ce}_2\text{Fe}_{17-x}\text{Co}_x\text{CN}$: A Combined Machine-Learning and *Ab Initio* Study

Anita Halder,¹ Samir Rom,¹ Aishwaryo Ghosh,² and Tanusri Saha-Dasgupta^{1,*}

¹*Department of Condensed Matter Physics and Material Sciences, S. N. Bose National Centre for Basic Sciences, JD Block, Sector III, Salt Lake, Kolkata, West Bengal 700106, India*

²*Department of Physics, Presidency University, Kolkata 700073, India*

 (Received 14 May 2020; revised 10 July 2020; accepted 7 August 2020; published 9 September 2020)

We employ a combination of machine learning and first-principles calculations to predict magnetic properties of rare-earth lean magnets. For this purpose, based on a training set constructed out of experimental data, the machine is trained to make predictions on magnetic transition temperature (T_c), largeness of saturation magnetization ($\mu_0 M_s$), and the nature of the magnetocrystalline anisotropy (K_u). Subsequently, the quantitative values of $\mu_0 M_s$ and K_u of the yet-to-be synthesized compounds, screened by machine learning, are calculated by first-principles density-functional theory. The applicability of the proposed technique of combined machine learning and first-principles calculations is demonstrated on 2-17-X magnets, $\text{Ce}_2\text{Fe}_{17-x}\text{Co}_x\text{CN}$. Further to this study, we explore the stability of the proposed compounds by calculating vacancy formation energy of small atom interstitials (N/C). Our study indicates a number of compounds in the proposed family and offers the possibility to become a solution for cheap and efficient permanent magnets.

DOI: [10.1103/PhysRevApplied.14.034024](https://doi.org/10.1103/PhysRevApplied.14.034024)

I. INTRODUCTION

Permanent magnets are a part of almost all technologies, starting from acoustic transducers, motors and generators, magnetic field and imaging systems to more recent technologies, such as computer hard-disk drives, medical equipment, magnetomechanics etc. [1]. The search for efficient permanent magnets is thus everlasting. In this connection, the family of rare-earth(RE)-and 3d-transition-metal (TM)-based intermetallics has evolved over the last 50 years or so and has transformed the landscape of permanent magnets [2,3]. Two of the most prominent examples of RETM permanent magnets, that are currently in commercial production, together with hard magnetic ferrites, are SmCo_5 and NdFe_{14}B .

While SmCo_5 and NdFe_{14}B provide reasonably good solutions, keeping in mind the resource criticality of RE elements like Nd and Sm, a significant amount of effort has been directed towards the search for permanent magnets without, or with less content of, critical RE elements. The idea is to optimize the price-to-performance ratio [2]. This has led to two routes: (a) the search for potential magnets devoid of rare-earth elements [4] and (b) the design of rare-earth lean intermetallics using abundant RE elements such as La and Ce instead of Sm and Nd [5–7]. As stressed by Coey [8], seeking low-cost magnets with a maximum

energy product to bridge ferrites and the presently used RE magnets is needed. Following route (b), cheap ternary and quaternary RE lean RETM intermetallics need to be investigated, since binaries have already been well explored. In parallel, due to Co being expensive, it may be worthwhile to focus on intermetallic compounds containing Fe.

Starting from the simplest binary RETM structure of CaCu_5 , by replacing n out of m RE (R) sites with a pair of TM (M) sites, $R_{m-n}M_{5m+2n}$ structures are obtained. This can give rise to several possible binary structures of different chemical compositions, listed in order of RE leanness; RM_{13} (7.1%), RM_{12} (7.7%), R_2M_{17} (10.5%), R_2M_{14} (12.5 %), RM_5 (16.7%), R_6M_{23} (20.7%), R_2M_7 (22.2 %), RM_3 (25%), RM_2 (33%) etc. Judging by the rare-earth content, 1:13, 1:12, 2:17, 2:14 compounds may form examples of rare-earth lean materials. It is desirable to modify the known binary compounds containing low-cost REs belonging to these families to achieve the best possible intrinsic magnetic properties, namely (i) high spontaneous or saturation magnetization ($\mu_0 M_s$), at least around 1 T, (ii) a Curie temperature (T_c) high enough for the contemplated device use, 600 K or above, and (iii) a mechanism for creating sufficiently high easy-axis coercivity (K_u). The synthesis and optimization of properties of real materials in experiment is both time consuming and costly, and is mostly based on trial and error. A computational approach in this connection is of natural interest to screen compounds, before they can be suggested and

*t.sahadasgupta@gmail.com

tested in laboratory. Typical computational approaches in this regard are based on density-functional-theory (DFT) calculations. A detailed calculation estimating all required magnetic properties, i.e., M_s , T_c , K_u from first principles is expensive and also not devoid of shortcomings. For example, estimation of T_c relies on parametrization of DFT or supplemented U -corrected theory of DFT+ U total energies to construct a spin Hamiltonian and a solution of the spin Hamiltonian by the mean field or Monte Carlo method. While this approach works for localized insulators, its application to metallic systems with itinerant magnetism is questionable, as it fails even for elemental metals, such as Fe, Co, and Ni [9]. A more reasonable approach of DFT+dynamical mean field (DMFT) [10] is significantly more expensive. An alternative approach is to use a machine-learning (ML) technique based on a suitable training dataset. This approach has been used for RETM permanent magnets based on a DFT-calculated magnetic properties database of M_s and K_u [5,11]. Creation of a database based on calculations, even with high-throughput calculations is expensive, and relies on the approximations of the theory. It is far more desirable to build a dataset based on experimental results, and then train the ML algorithm based on that. However, the size and availability of the experimental data in required format can be a concern. Focusing on the available experimental data on RE lean intermetallics, the set of T_c is largest, followed by that for K_u , and M_s . While the quantitative values of T_c in kelvins or degrees Celsius are available in the literature, for magnetocrystalline anisotropy often only the information about whether they are easy axis or easy plane is available. Similarly, the $\mu_0 M_s$ values are reported either in $\mu_B/\text{f.u.}$ or in emu/gm or in tesla, conversion from $\mu_B/\text{f.u.}$ and emu/gm to tesla requires information of the volume and density, which may introduce inaccuracies up to one decimal point. Restricting experimental data to those containing values of K_u and $\mu_0 M_s$ in the same format (either tesla or $\mu_B/\text{f.u.}$ or emu/gm) reduces the dataset of K_u and M_s significantly, making application of ML questionable. We thus use a two-pronged approach, as illustrated in Fig. 1. We first create a database of T_c , M_s , and K_u from the available experimental data on RE lean intermetallics, and use ML for prediction of T_c values, for estimating whether $\mu_0 M_s$ satisfies the criteria of being larger than 1 T, and for predicting the sign of K_u . For M_s and K_u , ML thus serves the purpose of initial screening. We next evaluate M_s and the magnetic anisotropy properties based on elaborate DFT calculations. Calculation of the magnetic anisotropy energy (MAE) is challenging due to its extremely small value. However, since the pioneering work of Brooks [12], several studies [6,13–15] have shown that U -corrected DFT generally reproduces the orientation and the right order of magnitude of the MAE.

We demonstrate the applicability of our proposed approach on Ce- and Fe-based 2:17 RETM intermetallics,

$\text{Ce}_2\text{Fe}_{17-x}\text{Co}_x$ compounds ($x = 1, \dots, 7$). Our choice is based on the following criteria: (a) the compounds contain rare-earth Ce, which is the cheapest within the RE family with a market price of approximately 5 USD/kg [16]. The cost of other components Fe, C, and N are all < 1 USD/kg. The price of Co is higher than Fe [16], being the less abundant metal. The Co:Fe ratio is thus restricted within 0.4. (b) Co substitution in place of Fe has been reported [17,18] to be efficient in simultaneous enhancements of K_u as well as T_c in several TM magnets. This is in sharp contrast to other TM substitutes, such as Ti, Mo, Cr, and V, where magnetic anisotropy as well as T_c are generally suppressed. (c) The search space belongs to the 2:17 family, which is the family in which most of the instances in our training set belongs to. (d) This class of compounds is found to be more stable than the well-explored 1:12 compounds. (e) For large saturation magnetization it is desirable to use Fe-rich compounds, which are also less expensive compared to Co. (f) Although Ce has a negative second-order Stefan factor, which favors in-plane MAE, experimental findings support that the nitrogenation and carbonation can switch the MAE from easy plane to easy axis [19]. (g) Although R_2Fe_{17} compounds display a large magnetization value due to high Fe content, these compounds are disadvantageous as they exhibit low Curie temperature [20]. The presence of Co, as well as C/N interstitials help in increasing T_c . (h) While magnetic properties of carbonitrides are expected to be similar to that of nitrides for sufficiently high concentration of N, carbonitride compounds have been proven to show better thermal stability [21].

Our study suggests that Fe-rich $\text{Ce}_2\text{Fe}_{17-x}\text{Co}_x\text{CN}$ compounds may form potential candidate materials for low-cost permanent magnets, satisfying the necessary requirements of a permanent magnet with $T_c > 600$ K, $\mu_0 M_s > 1$ T, and easy axis $K_u > 1$ MJ/m³. The calculated maximal energy product and estimated anisotropy field, which are technologically interesting figures of merit for hard-magnetic materials, turn to be within the reasonable range. Some of the studied compounds may possibly bridge the gap between the low maximal energy product and high anisotropy field for SmCo_5 and vice versa for $\text{Nd}_2\text{Fe}_{14}\text{B}$.

II. MACHINE-LEARNING APPROACH

A. Database construction and training of the model

Aiming to search not-yet-explored candidates for permanent magnets we use a supervised machine-learning (ML) algorithm, which helps us to screen compounds with high T_c ($T_c > 600$ K), high M_s ($\mu_0 M_s > 1$ T), and easy-axis anisotropy ($K_u > 0$) among the huge number of possible candidates of unexplored RETM intermetallics. The first step of any ML algorithm is to construct a dataset. We construct three datasets of existing RETM compounds for T_c , M_s , and K_u separately using the following sources: ICSD [22], the handbook of magnetic

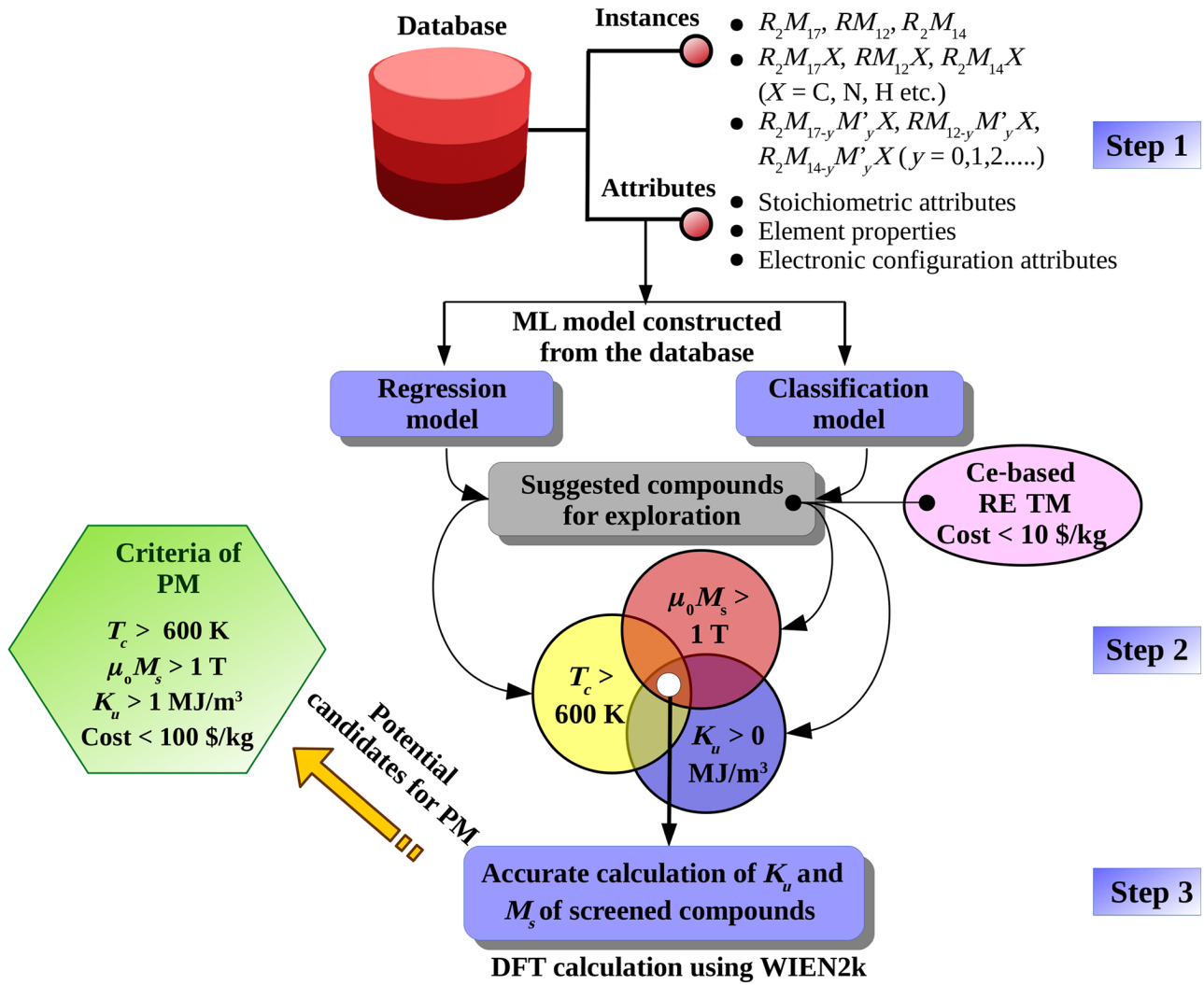


FIG. 1. Steps of a machine-learning-combined DFT approach for predictions of properties in $Ce_2Fe_{17-x}Co_xCN$ permanent magnets.

materials [23], the book of magnetism and magnetic materials [24], and other relevant references [19,21,25–78]. The datasets are presented in the Supplemental Material (SM) [79] as an easy reference for future users. To construct the database of rare-earth lean compounds, RE percentage in the intermetallic compounds is restricted to 14%, which includes the four different binary RETM combinations namely RM_{12} , RM_{13} , R_2M_{17} , and R_2M_{14} along with their interstitial and derived compounds. We discard RM_{13} from the dataset as only a few candidates are available from this series with known experimental T_c , M_s , and K_u .

We list a total of 565 compounds with reported experimental T_c , among which the majority of compounds (about 55%) belong to the R_2M_{17} series. The minimum contribution to the dataset comes from the R_2M_{14} (about 10%) family. The highest T_c in the dataset belongs to the R_2M_{17} class of compounds namely Lu_2Co_{17} [25] with $T_c \sim 1203$ K and the compound with the lowest T_c is $NdCo_{7.2}Mn_{4.8}$ (approximately 120 K) [23], a member from the RM_{12}

family. In the dataset all three compositions with RE to TM ratio 2:17, 2:14, and 1:12 show a large variation in T_c having the difference between maximum and minimum values as 1051, 775, and 991 K, respectively. There exists few compounds in the dataset with more than one reported value of T_c . For example T_c of $SmFe_{10}Mo_2$ has been reported with two different values of 421 K [80] and 483 K [81]. There are other examples of such multiple T_c [82–86]. The quality of the sample, their growth conditions, coexistence of compounds in two or multiple phases and accuracy of the measurements may lead to the multiple values of T_c reported for a particular compound. In such cases, we consistently consider the largest among the reported values of T_c . Notably in the majority of cases we find little variation in the reported values of T_c approximately 20–50 K).

The dataset of M_s is relatively smaller than T_c , containing only 195 entries. The majority of compounds in this dataset belong to the 2:17 composition similar to

the database of T_c . The relatively smaller dimension of the M_s dataset is primarily due to fact that experimental reports available for M_s are much less than T_c . Secondly, M_s has mostly been reported at room temperature, but in some cases at low temperature. To maintain uniformity of the dataset we consider M_s reported at room temperature, resulting in a lesser number of compounds in the M_s dataset.

Reports with quoted values of anisotropy constant are even more rare. Our exhaustive search resulted in only 73 data points. This pushes the dataset size to the limit of ML algorithms, for which predictive capability becomes questionable due to large bias masking the small variance [87]. On the other hand, if we also allow for experimental data, only reporting sign of K_u , this dataset gets expanded to a reasonable size of 258.

After constructing the dataset, we carry out preprocessing of the data, as outlined in Ref. [88]. It comprises the removal of noisy data, outliers, and correlated attributes. For details see the Appendix.

The next and most crucial step is to construct a set of simple attributes, which are capable of describing the instances (in this case RETM compounds) and then deploy the ML algorithm to map them to a target (in this case T_c , M_s , and K_u). The attributes considered in this study are summarized in Table I, which can be divided into three broad categories, namely, stoichiometric attributes, element properties, and electronic configuration attributes. The stoichiometric attributes may contain information of both elemental and compositional properties as suggested

TABLE I. List of 13 different attributes with description, notation, and range used in the ML algorithm. Here “CW” stands for “composition-weighted.”

Attribute type	Attribute	Notation	Value range
Stoichiometric	CW absolute deviation of atomic no.	$\langle \Delta Z \rangle$	1.70-16.74
	CW av. of atomic no. of TM	$\langle Z_{TM} \rangle$	10-33.30
	CW av. of atomic no. of LE	$\langle Z_{LE} \rangle$	0-9.79
	CW av. Z	$\langle Z \rangle$	21.08-37.71
	CW electronegativity diff. of RE and TM	$\Delta\epsilon$	0.61-1.84
	CW RE percentage	RE%	4.76-14.29
	CW TM percentage	TM%	38.46-95.24
	CW LE percentage	LE%	0-53.85
	Element	Atomic no. of RE	Z_{RE}
Presence of more than one TM		N_{TM}	yes/no
Presence of LE		N_{LE}	yes/no
Electronic	Total no. of f electrons	f^n	1-28
	Total no. of d electrons	d^n	30-136

by Ward *et al.* [89]. This is based on taking compositional weights (CW) of elemental properties.

In the third step, we train different popular machine-learning algorithms with the constructed dataset for prediction. We use the ML algorithm in three different problems: (a) to predict the compounds with T_c more than 600 K, (b) compounds with $\mu_0 M_s > 1$ T, and (c) compounds with easy-axis anisotropy. Regression is used in the former case, whereas the latter two cases are treated as classification problems. We use five different ML algorithms for regression in the case of T_c namely ridge regression (RR) [90], kernel ridge regression (KRR) [91], random forest (RF) [92,93], support vector regression (SVR) [94], and artificial neural network (ANN) [95]. The details can be found in the Appendix. Out of the five different ML algorithms, it is seen that random forest performs best, which has also been successfully used for prediction of Heusler compounds [96], half-Hausler compounds [97], double perovskite compounds [88], half-Heusler semiconductor with low thermal conductivity [98], zeolite crystal-structure classification [99] etc. Results presented in the following are based on the random-forest method.

B. Model evaluation

The final step is to employ the trained algorithm on yet-to-be synthesized RETM compounds, and thus to explore unexplored compositions with targeted properties. We choose $\text{Ce}_2\text{Fe}_{17-x}\text{Co}_x\text{C}_y\text{N}_z$ ($y, z = 0/1$; $x = 0 \dots 8$) as the exploration set for application of the trained ML algorithm. This results in a set of 36 compounds among which eight compositions ($\text{Ce}_2\text{Fe}_{17-x}\text{Co}_x\text{CN}$, $x = 1, \dots, 8$) have not been reported experimentally or theoretically. We apply our trained ML algorithms on all of these 36 compounds and the results are summarized in Fig. 2. The top panel of Fig. 2 shows the predicted T_c of all the compounds. It is seen that the nitrogenation or carbonation increases the T_c with respect to their respective parent compound $\text{Ce}_2\text{Fe}_{17-x}\text{Co}_x$. Our ML model predicts that the nitrides have higher T_c than that of the carbides. For $x \leq 5$, the enhancement of T_c is maximum for the compounds where both carbon and nitrogen are present. For $x > 5$, T_c shows a slight decrease compared to only the nitrogenated case. It is also noted that the relative rise in T_c in interstitial compounds compared to parent compounds, decays gradually with Co concentration. The increase in T_c varies from approximately 200 to 10 K as x varies from 0 to 8 for carbides and nitrides whereas introduction of both nitrogen and carbon shows the variation from approximately 310 to 30 K. Our result reproduces the trend of experimental findings in a qualitative manner. The experimental results for $x = 0$ ($\text{Ce}_2\text{Fe}_{17}$) [100,101], concluded that the enhancement in T_c is highest in the presence of both carbon and nitrogen [102,103] ($T_c \sim 721$ K), followed by the

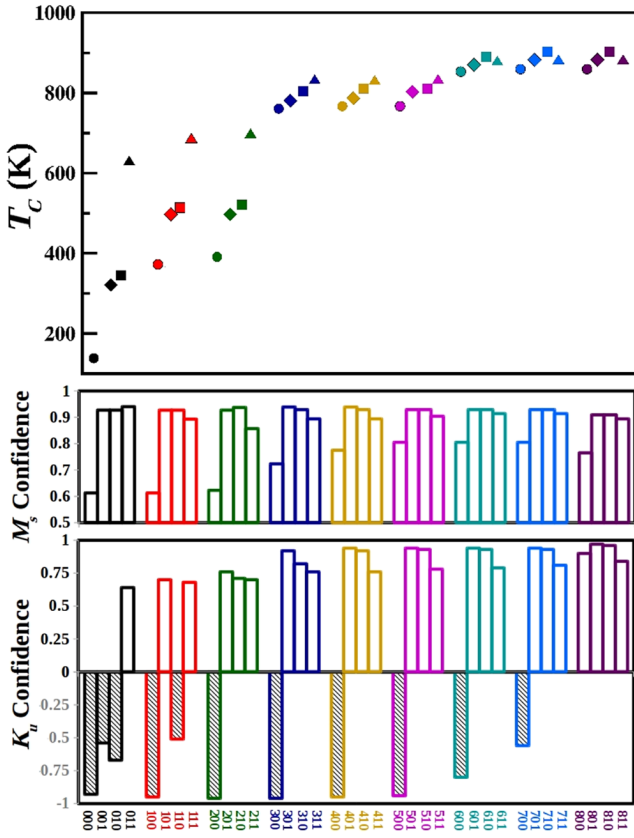


FIG. 2. ML predictions of Curie temperature (T_c) from regression model, and saturation magnetization (M_s) and anisotropy constant (K_u) from classification model. The upper (middle/lower) panel shows the results of T_c (M_s/K_u). The exploration set is $\text{Ce}_2\text{Fe}_{17-x}\text{Co}_x\text{C}_y\text{N}_z$ where y and z can have values either 0 or 1, and $x = 0 \dots 8$, acronymed as xyz . In the top panel, noninterstitial compounds, carbonated, nitrogenated and carbonitrogenated compounds are symbolized by circle, diamond, square and upper triangle. Different colors specify compounds with different x values. The middle panel shows the ML prediction confidence for M_s . In the lower panel, ML prediction confidence for K_u is illustrated. Here the upper (lower) half having bars with no-fill (shaded) shows the confidence for the compounds with positive (negative) K_u .

nitrogenated compound [104,105] ($T_c \sim 700$ K) and lowest for the carbonated compound [102,103] ($T_c \sim 589$ K). Though it is not possible to compare the results quantitatively as the stoichiometry of the experimentally studied carbonated and nitrogenated compounds are not the same as in our exploration dataset, the overall trend is similar. We also find that our ML model underestimates the T_c of the pure binary compound $\text{Ce}_2\text{Fe}_{17}$ [20]. This is expected, as already discussed, our model is less precise for the prediction of low T_c compounds.

Switching to the M_s part, the middle panel of Fig. 2 shows the confidence of classification of compounds with $\mu_0 M_s$ more than 1 T. The confidence value closer to 1 implies that the prediction is viable to be more accurate.

All the compounds are classified in favor of forming permanent magnets with $\mu_0 M_s > 1$ T. For compounds like $\text{Ce}_2\text{Fe}_{17-x}\text{Co}_x$ the prediction confidence varies from 0.6 to 0.8 with increasing Co concentration, whereas the carbon and nitride compounds are always classified with high prediction confidence.

The predictions from the classification model on K_u is shown in the bottom panel of Fig. 2. We find while the anisotropy of $\text{Fe}_{17-x}\text{Co}_x$ compounds without interstitial C/N ($x = 2, \dots, 7$) atoms are predicted to be easy plane, their carbonated or nitrogenated or carbonitrogenated counterparts show easy-axis anisotropy. For pure Fe compounds, apart from the carbonitrogenated compound, all are predicted to be easy plane, while for Fe_{16}Co compounds carbonated as well as carbonitrogenated compounds are predicted to be easy axis. This in turn, highlights the effectiveness of Co substitution on making K_u positive. We note the prediction confidence of the carbonitrogenated compounds is around 0.75.

On the basis of the above ML analysis, we pick up seven yet-to-be synthesized compounds, $\text{Ce}_2\text{Fe}_{17-x}\text{Co}_x\text{CN}$, $x = 1, \dots, 7$. This choice is guided by the compounds satisfying $T_c > 600$ K from the regression model, and $\mu_0 M_s > 1$ T with easy-axis anisotropy from classification models, and being Fe rich. In the following, we describe their crystal structure, and present results of DFT-calculated electronic structure, anisotropy properties, and stability properties.

III. DFT-Calculated Properties of Predicted Compounds

A. Crystal Structure

The $\text{Ce}_2\text{Fe}_{17}$ compounds crystallize in the rhombohedral $\text{Th}_2\text{Zn}_{17}$ -type structure (space group $R\bar{3}m$), derived from the CaCu_5 -type structure with a pair (dumbbell) of Fe atoms for each third rare-earth atom in the basal plane and the substituted layers stacked in the sequence ABCABC \dots . As shown in Fig. 3, the transition metal atoms are divided into four sublattices, $9d$, $18f$, $18h$, and $6c$, having 3 (9), 6 (18), 6 (18), and 2 (6) multiplicity in the one (three) formula unit primitive-rhombohedral (hexagonal) unit cell. The TM atoms occupying the $6c$ sites, referred to as dumbbell sites, form the \dots -TM-TM-RE-RE- \dots chains running along the c axis of the hexagonal cell. The $18f$ TM atoms form a hexagonal layer, which alternates with the hexagonal layer formed by $9d$ and $18h$ TM atoms. The $6c$ TM-TM dumbbells pass through the hexagons formed by $18f$ TMs. For the interstitial C and N atoms, neutron powder diffraction [106], EXAFS experiments confirmed that they fill voids of nearly octahedral shape formed by a rectangle of $18f$ and $18h$ TM atoms and two RE atoms at opposite corners, which are the $9e$ sites of $\text{Th}_2\text{Zn}_{17}$ -type structure, and having the shortest distance from the RE

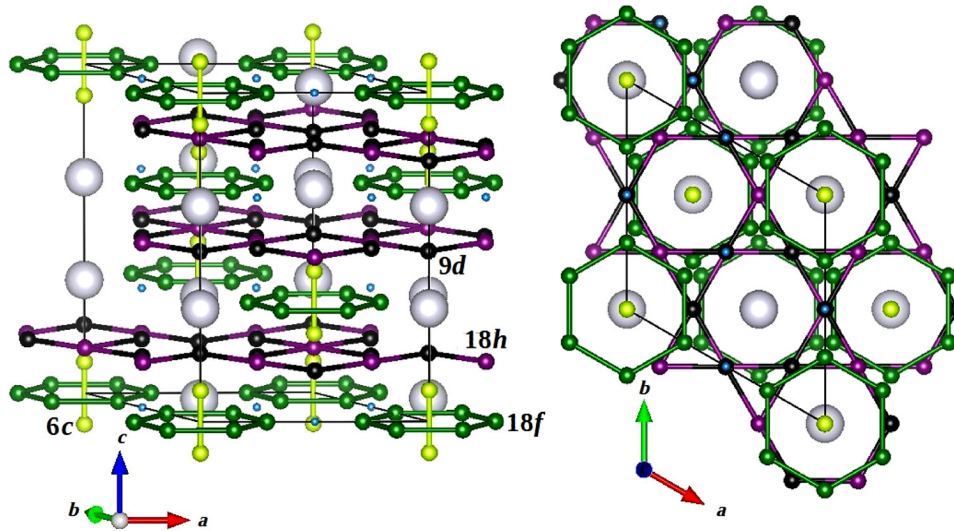


FIG. 3. Crystal structure of $\text{Ce}_2\text{Fe}_{17-x}\text{Co}_x\text{CN}$ magnets. The Ce, Fe/Co and C/N atoms are shown with large, medium and small balls, respectively. Four transition metal sublattices $9d$, $18f$, $18h$ and $6c$ are shown in black, green, magenta and yellow colored balls, respectively. Left panel shows the crystal structure viewed with c -axis pointed vertically up and the right panel shows the crystal structure viewed along the c -axis.

sites among all available interstitial sites. All our calculations are thus carried out with C/N atoms in $9e$ positions. The RE atoms in $6c$ position as well as light elements C/N in $9e$ interstitial sites belong to the same layer as $18f$ TMs. As the $9e$ sites are in the same c plane as the RE sites, having RE atoms as neighbors, introduction of interstitials like C and N is expected to have a profound influence on the electronic environment of RE atoms, thereby altering the magnetocrystalline anisotropy.

Although the $R\bar{3}m$ symmetry is lowered upon Co substitution and the spin-orbit coupling (SOC) in the anisotropy calculation, for the ease of identification, we still use the notations $9d$, $18f$, $18h$, and $6c$. Our total energy calculations show that Co preferentially occupy sites in the sequence $9d > 18h > 6c > 18f$. Out of the available 17 TM sites we consider Co substitution up to seven sites, which result in Fe-rich phases of compositions $\text{Ce}_2\text{Fe}_{17-x}\text{Co}_x\text{CN}$ with $x = 1, 2, \dots, 7$. Following the site preference we consider Co atoms in $9d$ and $18h$ sites.

We expect the lattice parameters not to change much upon Co substitution, as Fe and Co, being neighboring elements in the periodic table, have similar atomic radii. Nevertheless, to check the influence of Co substitution on lattice structure, we optimize the lattice constant and the volume for all x values. Following our expectation, the results only show a marginal decrease in lattice parameter and volume (with a maximum deviation of 1%) upon increasing Co content, in line with the findings by Odkhuu *et al.* [18] for 1:12 compounds, and the experimental findings by Xu and Shaheen on 2:17 compounds [19]. This minimal change is found to have no appreciable effect on magnetic properties, as explicitly checked on representative compounds with $x = 1, 4$, and 7 . We thus choose the lattice structure as the optimized lattice structure of $x = 0$ (see Appendix), with lattice constant = 6.59 \AA and

angle $\beta = 83.3^\circ$ of the rhombohedral unit cell [107] in subsequent calculations.

B. Magnetic Moment and Electronic Structure

In the following we present the DFT results for the magnetic moments and density of states (DOS), as given in generalized-gradient approximation (GGA)+ U +SOC calculations. The details of the DFT calculations are presented in the Appendix. The importance of the application of supplemented Hubbard U on RE sites within LDA or GGA+ U formalism is considered as one of the possible means to deal with localized f orbitals of RE ions, and has shown to provide reasonable description [13,14]. Previous calculations in compounds containing Ce, showing variations of U within 3 to 6 eV, keeps the results qualitatively the same [6,108]. In the following, we present results for U applied on Ce atoms chosen to be 6 eV.

Figure 4 shows the calculated total magnetic moments of the seven mixed Fe-Co compounds, $\text{Ce}_2\text{Fe}_{17-x}\text{Co}_x\text{CN}$ ($x = 1, 2, \dots, 7$). The total magnetic moment shows a decreasing trend with an increase of Co concentration, arising from the fact that Co moment is smaller than that of Fe. However, it is reassuring to note that even for the compound with the largest Co concentration, $\text{Ce}_2\text{Fe}_{10}\text{Co}_7\text{CN}$, the calculated moment is more than 1.65 T. This is in agreement with ML prediction, which predicts $\mu_0 M_s$ of all the considered compounds to be larger than 1 T, though it is to be noted the ML predictions are made for room-temperature moments while the DFT-calculated moments are at $T = 0 \text{ K}$. The measured values of total moment in corresponding nitrogenated compounds show good comparison (cf. Fig. 4) with our calculated moments. In particular, barring the data on $x \approx 2$, the other two data points show good matching with the trend of theoretical results. We note that the experimentally determined moments are

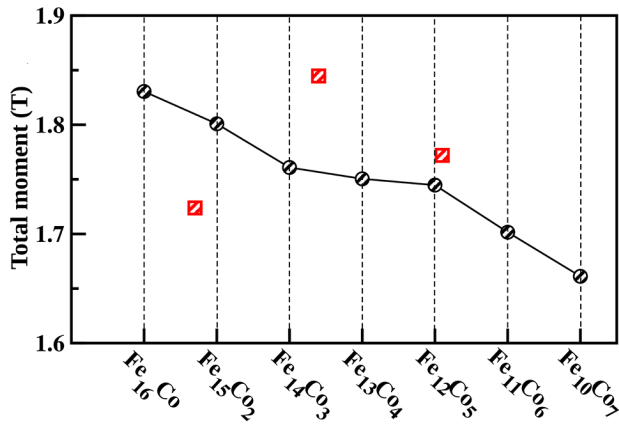


FIG. 4. Calculated total moment (black circles), $\mu_0 M$ in T plotted for increasing Co concentrations of $\text{Ce}_2\text{Fe}_{17-x}\text{Co}_x\text{CN}$ compounds. Experimental results are also shown [19] (red, square) for $\text{Ce}_2\text{Fe}_{17-x}\text{Co}_x\text{N}_y$ compounds measured at room temperature. For comparison between $T = 0$ K calculated moments, and experimental data measured at room temperature, the experimental data has been scaled by a factor of 1.3.

for $\text{Ce}_2\text{Fe}_{17-x}\text{Co}_x\text{N}_y$ compounds, which only contain N as an interstitial atom, and the value of y is not mentioned, which may even vary depending on the value of x .

Figure 5 shows the spin and orbital moments projected to Ce, Fe(9d), Fe(18f), Fe(18h), Fe(6c), and Co atoms for the representative case of the $\text{Ce}_2\text{Fe}_{15}\text{Co}_2\text{CN}$ compound. The results for other Co concentrations are similar. In the presence of large SOC at the Ce site, a substantial orbital moment develops, which is oppositely aligned to its spin moment following Hund's rule. Considering 3+ nominal valence of Ce, it would be in $4f^1$ state, with $S = 1/2$ and $L = 3$. While the calculated value of the Ce spin moment is close to $1 \mu_B$ (approximately equal to $0.95 \mu_B$) in accordance with nominal $S = 1/2$ state, the orbital moment shows significant quenching with a calculated value of about $0.5 \mu_B$. This value of orbital moment is in agreement with DFT-calculated values of other Ce containing RETM magnets [6,109]. The $4f$ electrons are coupled to $5d$ electrons at the Ce site by intra-atomic exchange interaction, following which their spin moments are aligned in parallel direction. The delocalized $5d$ electrons at the Ce site, hybridize with Fe or Co $3d$ electrons, favoring antiparallel alignment of Ce and Fe or Co spins, as found in Fig. 5. The spin magnetic moment at Fe sites shows a distribution, with Fe at the 6c site having the largest moment, followed by Fe at 9d and 18h sites while Fe at the 18f site shows the lowest moment. We notice that Fe (6c) atoms occupying the dumbbell sites, have less connectivity compared to Fe(9d), Fe (18f), and Fe (18h), and thus possess the largest moment, being of most localized character. Among Fe (9d), Fe(18f), Fe(18h) sites Fe (18f) has the smallest moment, driven by the fact that interstitial C and N atoms are in same plane as Fe (18f) causing enhanced

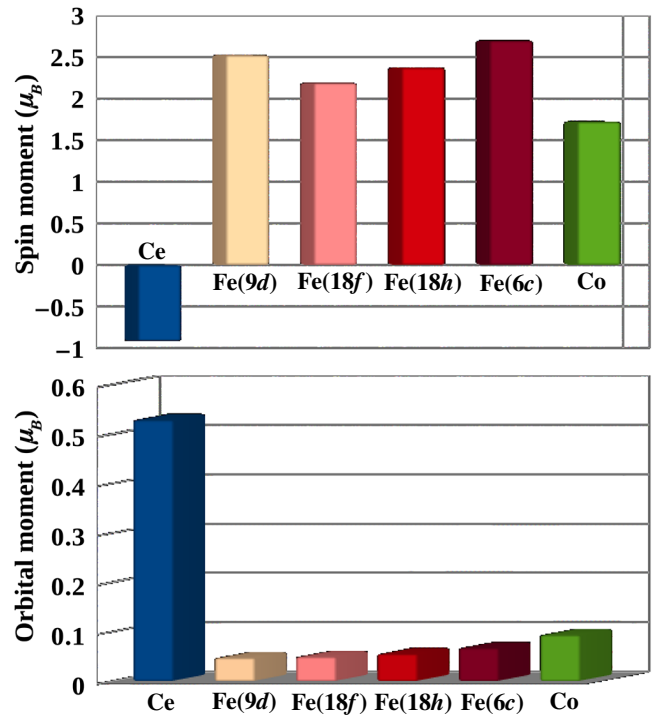


FIG. 5. Calculated spin (top) and orbital (bottom) moments at Ce, Fe(9d), Fe(18f), Fe(18h), Fe(6c), and Co sites in the representative case of $\text{Ce}_2\text{Fe}_{15}\text{Co}_2\text{CN}$ compound.

d - p hybridization, and reduction in moment. These spin moments though are larger than that of bulk Fe (approximately equal to $2.2 \mu_B$). The orbital moment at Fe sites are tiny (approximately equal to $0.05 \mu_B$). In comparison, Co shows significantly smaller spin moment (approximately equal to $1.7 \mu_B$) and somewhat larger orbital moment (approximately equal to $0.1 \mu_B$), justifying the fall in total moment with increasing concentration of Co.

Figure 6 shows the density of states of $\text{Ce}_2\text{Fe}_{15}\text{Co}_2\text{CN}$, projected to various orbital characters. The Ce $4f$ states are all unoccupied in the majority spin channel, partly occupied in the minority spin channel, in accordance with nominal f^1 occupancy. The RE $4f$ -TM $3d$ hybridization through empty RE $5d$ states is visible, making the spin splitting at Fe and Co sites antiparallel to that of Ce. The C/N p states mostly spanning the energy range -7 to -4 eV, show nonnegligible mixing with Fe d , Co d , and Ce f characters, justifying their role in influencing the magnetic properties. Fe d and Co d states span about the same energy range from -4 to 2 eV, with states mostly occupied in the majority spin channel and partially occupied in the minority spin channel, largely accounting for the metallicity of the compound. Spin splitting of Fe d is larger than that of Co, being consistent with the larger magnetic moment of Fe compared to Co. Projection to different inequivalent Fe sites (cf. the right panel of Fig. 6), Fe(9d), Fe(18h), Fe(18f), and Fe(6c) show that Fe(6c) belonging to the

dumbbell pair is distinct from the other Fe sites, which also exhibit the largest magnetic moment among all Fe's.

C. Magnetocrystalline Anisotropy

Having an understanding of the basic electronic structure, in terms of magnetic moments and density of states, we next focus on calculation of magnetocrystalline anisotropy constant, K_u , which is a crucial quantity responsible for coercivity in a permanent magnet. MAE defines the energy required for turning the orientation of the magnetic moment under applied field, expressed as $E(\theta) \approx K_1 \sin^2 \theta + K_2 \sin^4 \theta + K_3 \sin^4 \theta \cos 4\phi$, where K_1 , K_2 , and K_3 are the magnetic anisotropy constants, θ is the polar angle between the magnetization vector and the easy axis (c axis), and ϕ is the azimuthal angle between the magnetization component projected onto the a - b plane and the a axis. In most cases, the higher-order term K_3 is relatively small compared with K_1 and K_2 . For $\theta = \pi/2$, one may thus write $K_u \approx K_1 + K_2$. Its positive and negative values indicate the easy-axis and easy-plane anisotropy, respectively. To satisfy the criteria of a good permanent magnet, it should have easy-axis anisotropy with a value larger than 1 MJ/m^3 [2,8]. The MAE in RETM arises from two contributions: (i) MAE of the RE sublattice due to strong spin-orbit coupling and crystal-field effect and (ii) MAE of the TM sublattice. The interplay of the two decides the net sign and magnitude. In particular, in the proposed compounds, the presence of Co with a significant value of orbital moment makes the contribution of the TM sublattice noteworthy. While 2:17 compounds, primarily show easy-plane anisotropy, switching to easy-axis anisotropy for interstitial compounds has been reported. In particular, upon nitrogenation, easy-plane anisotropy has been reported for Ce containing mixed Fe-Co compounds [19]. As mentioned already, the interstitial atoms occupy the

same plane as the RE atoms, significantly influencing their properties. With predicted high T_c and large saturation moment of our proposed compounds with carbonation and nitrogenation, it remains to be seen whether they exhibit easy-axis anisotropy of reasonable values, as required for a legitimate candidate for permanent magnet. For this purpose, we carry out calculations within GGA+ U +SOC with the magnetization axis pointing along the crystallographic c axis and perpendicular to it. The significance of the application of U on the proper description of MAE in terms of its sign and order of magnitude has been stressed upon by several authors [6,13]. In order to establish our method on the calculation of MAE involving a small energy difference, we first apply our method to the known and well-studied case of SmCo_5 , with choice of $U = 6 \text{ eV}$ on Sm, and obtain a MAE value of 24.4 meV/f.u. , which agrees well with the GGA+ U +SOC-calculated value of 21.6 meV/f.u. , reported in the literature [13] as well as experimentally measured values of $13\text{--}16 \text{ meV/f.u.}$ [110]. The calculated results for the proposed $\text{Ce}_2\text{Fe}_{17-x}\text{Co}_x\text{CN}$ are shown in the top panel of Fig. 7. We find that MAE shows site dependence on the Co substitution. We consider configurations with Co atoms substituting Fe(9d) and Fe(18h) sites, configurations involving other substituting sites being energetically much higher. We consider configurations that are energetically close (within 600 K) and calculate the Co-composition-dependent MAE using the virtual crystal approximation. Specifically, for $x = 1$ we consider configurations $\text{Co@Fe}(9d)$ and $\text{Co@Fe}(18h)$, the latter being 3.58 meV higher compared to the former. Similarly for $x = 2$, we consider $\text{Co@}2 \times \text{Fe}(9d)$ and $\text{Co@}2 \times \text{Fe}(18h)$, the latter being 4.43 meV higher compared to the former. For $x = 3$, the configurations considered are $\text{Co@}2 \times \text{Fe}(9d) + \text{Fe}(18h)$; $\text{Co@}3 \times \text{Fe}(9d)$; $\text{Co@Fe}(9d) + 2 \times \text{Fe}(18h)$, the energies being 0 meV (set as zero of energy), 12.37 meV and 47.66 meV , respectively. For $x =$

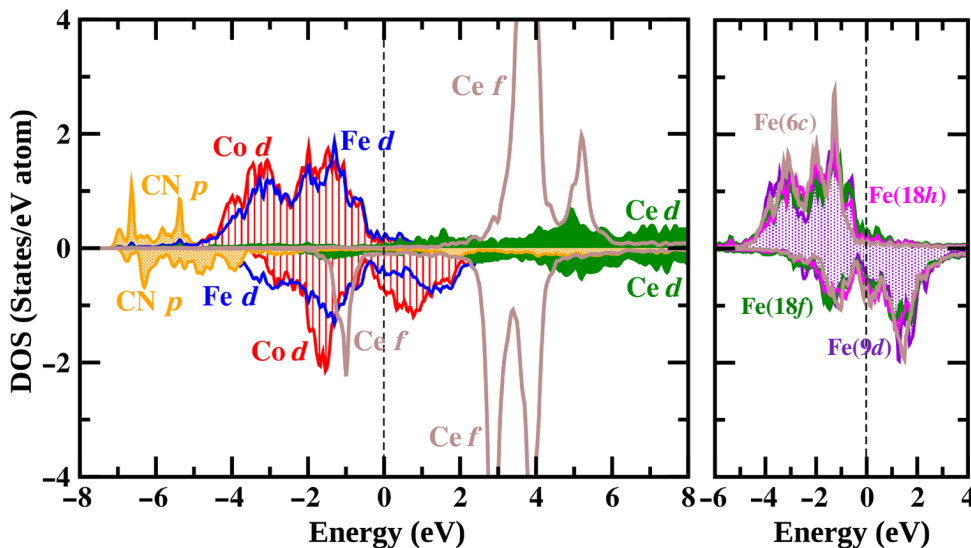


FIG. 6. Left: density of states of the $\text{Ce}_2\text{Fe}_{15}\text{Co}_2\text{CN}$ compound, projected onto Ce f (brown), Ce d (shaded green), Fe d (blue), Co d (shaded red), and CN p (shaded orange) characters. Right: density of states of the $\text{Ce}_2\text{Fe}_{15}\text{Co}_2\text{CN}$ compound projected to different Fe d 's: Fe(9d) (shaded indigo), Fe(18h) (magenta), Fe(18f) (green), and Fe(6c) (brown). The zero of the energy is set at Fermi energy.

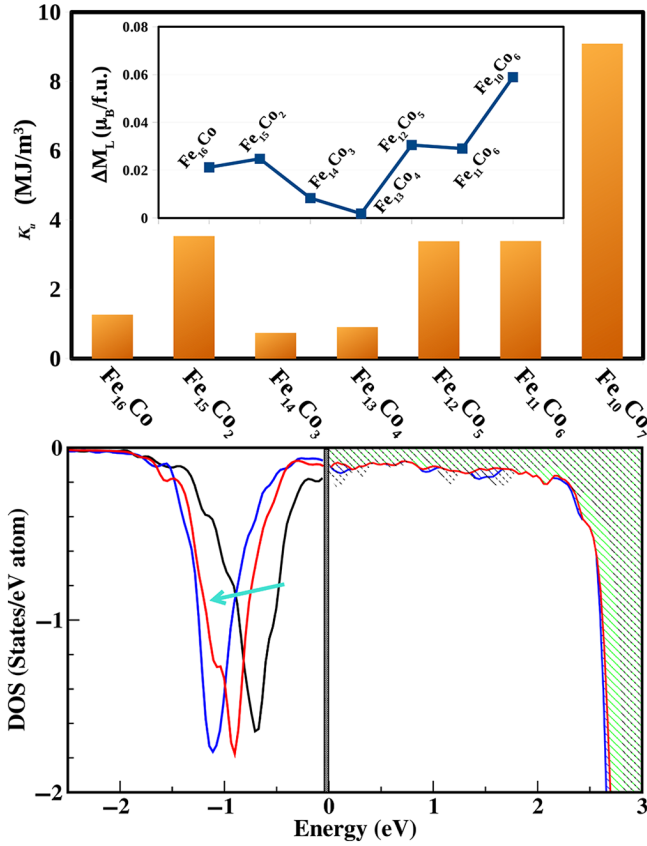


FIG. 7. Top: calculated magnetocrystalline anisotropy constant in MJ/m³ plotted for increasing Co concentrations of Ce₂Fe_{17-x}Co_xCN compounds. The inset shows the anisotropy in orbital moment (see text for details). Bottom: the GGA+U+SOC DOS projected to Ce *f* energy states with magnetization axis pointed along easy axis, for Ce₂Fe₁₇ (black), Ce₂Fe₁₇CN (red), and Ce₂Fe₁₆CoCN (blue). The zero of the energy is set at Fermi energy, with the unoccupied part shown as shaded. The arrow indicates the shift in the occupied part.

4, the configurations considered are Co@2 × Fe(9*d*) + 2 × Fe(18*h*); Co@3 × Fe(9*d*) + Fe(18*h*), the energies being 0 meV (set as zero of energy) and 36.5 meV, respectively. For $x = 5, 6$, and 7 , only one configuration is considered, others being energetically much higher, namely, Co@3 × Fe(9*d*) + 2 × Fe(18*h*), Co@3 × Fe(9*d*) + 3 × Fe(18*h*), and Co@3 × Fe(9*d*) + 4 × Fe(18*h*), respectively.

Considering the spin-orbit effect only on the Ce atom, it is found to account for about 60% of the calculated MAE. We find all the calculated MAE is positive, in good agreement with ML prediction on mixed Fe-Co carbonitride compounds. Further MAE values show non-monotonic dependence on Co concentration. Such a non-monotonic trend upon varying TM content has also been reported in the context of $R(\text{Fe}_{1-x}\text{Co}_x)_{11}\text{TiZ}$ ($R = \text{Y}$ and Ce ; $Z = \text{H}, \text{C}$, and N) [7] and RETM systems in general [111]. In the inset of the top panel of Fig. 7, we show the calculated orbital magnetic anisotropy (ΔM_L) defined as

$\Delta M_L = M_L(a) - M_L(c)$, as employed in Ref. [18], $M_L(c)$ and $M_L(a)$ being the orbital moment along the *c* axis and *a* axis, respectively. We find a correlation between ΔM_L and K_u , qualitatively satisfying Bruno’s expression [112] for itinerant ferromagnets given as $K_u = (\xi/4\mu_B)\Delta M_L$, where ξ is the strength of SOC.

Most of the easy-axis K_u values are found to be larger than 1 MJ/m³, except Fe₁₄Co₃ and Fe₁₃Co₄ for which it is found to be 0.74 and 0.91 MJ/m³, respectively. Few of the concentrations exhibit easy-axis K_u values larger than 2 MJ/m³, e.g., Fe₁₅Co₂ (3.54 MJ/m³), Fe₁₂Co₅ (3.39 MJ/m³), Fe₁₁Co₆ (3.39 MJ/m³), Fe₁₀Co₇ (9.10 MJ/m³), being comparable to Nd₂Fe₁₄B (4.9 MJ/m³) [113].

To obtain microscopic understanding of the role of Co substitution and doping by C, N on magnetocrystalline anisotropy, we further calculate the magnetocrystalline anisotropy of Fe-only compounds Ce₂Fe₁₇, Ce₂Fe₁₇C, Ce₂Fe₁₇N, and Ce₂Fe₁₇CN. This results in negative K_u values for Ce₂Fe₁₇, and Ce₂Fe₁₇C (−2.12 MJ/m³ and −1.35 MJ/m³), a tiny positive value for Ce₂Fe₁₇N (0.26 MJ/m³) and positive value for the codoped compound Ce₂Fe₁₇CN (1.27 MJ/m³). We further plot the GGA+U+SOC density of states (cf. bottom panel, Fig. 7) with magnetization axis along the *c* axis projected to Ce *f* states for Ce₂Fe₁₇, Ce₂Fe₁₇CN, and Ce₂Fe₁₆CoCN, which is expected to reveal the mechanism of uniaxial anisotropy. We find that a lowering of occupied Ce *f* energy states and increase in band width occur upon introduction of light elements C and N. This gets further helped by substitution of Co, caused by hybridization between Ce *f* states and Co *d* and C,N *p* states. This gain in hybridization energy stabilizes easy-axis magnetization (cf. Ref. [114]) as observed experimentally [19].

D. Maximal energy product and anisotropy field

While the estimates of K_u and $\mu_0 M_s$ are useful information to access the effectiveness of the suggested materials as permanent magnets, technologically interesting figures of merit of hard magnetic materials, are the maximal energy product $(\text{BH})_{\text{max}}$ and anisotropy field H_a . These can be estimated from the knowledge of $\mu_0 M_s$ and K_u as follows:

$$(\text{BH})_{\text{max}} = \frac{(0.9 \mu_0 M_s)^2}{4\mu_0},$$

$$H_a = \frac{2K_u}{\mu_0 M_s}.$$

The factor 0.9 in the expression for $(\text{BH})_{\text{max}}$ implies the common assumption that ideally 10% of a processed bulk hard magnet consists of nonmagnetic phases [115]. The estimated $(\text{BH})_{\text{max}}$ and H_a is shown in Fig. 8. The $(\text{BH})_{\text{max}}$ value is found to range from 444 to 540 kJ/m³, in comparison to experimentally measured values 516 kJ/m³ and 219

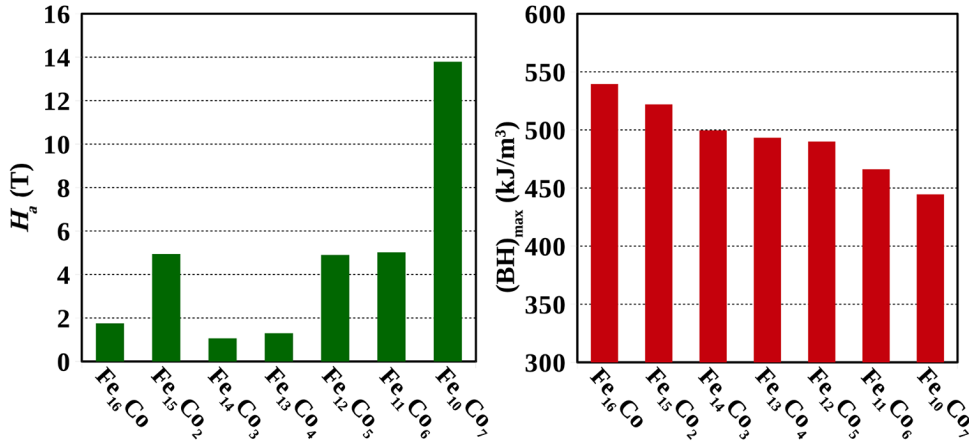


FIG. 8. Calculated anisotropy field in tesla (left) and maximal energy product in kJ/m³ (right) plotted for increasing Co concentrations of Ce₂Fe_{17-x}Co_xCN compounds.

kJ/m³ for Nd₂Fe₁₄B [116] and SmCo₅ [116], respectively. The H_a shows a strong variation with Co concentration, ranging from approximately 1 to 14 T [117].

We further note that the hardness parameter, defined as $\kappa = \sqrt{K_u/\mu_0 M_s^2}$, turns out to be greater than 1 for Ce₂Fe₁₅Co₂CN, Ce₂Fe₁₂Co₅CN, Ce₂Fe₁₁Co₆CN, and Ce₂Fe₁₀Co₇CN compounds, employing the calculated $T = 0$ K values of K_u and M_s .

E. Stability

Unlike the other RETM magnets like 1:12 compounds, one of the advantages of 2:17 compounds is their stability. Both the stable form of Ce₂Fe₁₇ and its Co substituted form have been reported in the literature [19]. Calculation of formation enthalpies, as given in Ref. [18], $E_{\text{form}} = (E_{\text{compound}} - \sum_k N_k \epsilon_k) / \sum_k N_k$, where N_k indicate the number of different atoms (Ce, Fe, Co, N, and C) in the cell, and ϵ_k denote the energy and atom of bulk Ce in fcc structure, α -Fe, Co in HCP structure, in molecular nitrogen and C in graphite structure, gives values -0.61 to -0.59 eV/atom for the studied Ce₂Fe_{17-x}Co_xCN compounds.

A major challenge with interstitial compounds, though, is the nitrogen diffusion [21]. It has been further suggested the blockage of nitrogen diffusion by carbon layer is useful in reduction of nitrogen outgassing in carbonitrides. In particular, heating up Sm₂Fe₁₇ carbonitrides at a constant rate

TABLE II. Vacancy formation energy for carbon [$\Delta E_f(C)$], nitrogen [$\Delta E_f(N)$] and nitrogen-carbon [$\Delta E_f(CN)$] in eV in Ce₂Fe_{17-x}Co_xCN compounds.

	$\Delta E_f(CN)$	$\Delta E_f(N)$	$\Delta E_f(C)$
$x = 1$	4.32	2.10	0.97
$x = 2$	3.99	2.09	0.85
$x = 3$	4.16	2.09	0.88
$x = 4$	3.98	2.10	0.79
$x = 5$	3.82	2.07	0.70
$x = 6$	3.91	2.05	0.72
$x = 7$	3.78	2.01	0.69

in a differential scanning calorimeter, the onset temperature of nitrogen outgassing is found to be higher by more than 40 K, as compared to the nitride counterpart [21] This justifies the choice of carbonitrides as our exploration set. To this end, we calculate the vacancy formation energy of the interstitial atoms in our chosen compounds. For this purpose, we calculate the formation energy of the N and/or C vacancy (ΔE_f) defined as

$$\Delta E_f = E^{N(C)\text{vac}} - E^{\text{pristine}} + E_{N(C)},$$

where $E^{N(C)\text{vac}}$ and E^{pristine} denote the optimized total energies of the compound containing N and/or C vacancy, and the vacancy-free compound. The internal positions for defect-free pristine structure and structures containing nitrogen and/or carbon vacancies are performed keeping the lattice parameters fixed. $E_{N(C)}$ is the energy per N or C atom, which is obtained from calculation of N₂ molecule or graphite. The obtained results for Ce₂Fe_{17-x}Co_xCN compounds in minimum energy configuration of Co is shown in Table II. The vacancy formation energies show hardly any variation on the chosen configuration for a given Co concentration.

The vacancy formation energies, listed in Table II, show only small variation between compounds of varying Co concentration, with the general trend $\Delta E_f(CN) > \sum [\Delta E_f(N) + \Delta E_f(C)]$. The individual nitrogen-vacancy formation energy and carbon-vacancy formation energy, are in overall agreement with that found for related compound, SmCaFe₁₇C(N)₃ [6]. The vacancy formation energy for codoped carbon-nitrogen compounds are found to be enhanced by about 35–40% compared to the sum of the individual C and N vacancy formation energies, proving the carbonitrogenation codoping to provide better thermal stability. We also check our results by repeating vacancy formation energy calculations for $x = 0$ compounds, which however do not show significant difference, suggesting Co doping does not have a major role in stability, as also indicated by no significant variation of results between $x = 1, 2, 3, 4, 5, 6,$ and 7 .

IV. Conclusion

Designing alternative solutions for permanent magnets, satisfying the criteria of low cost while keeping the magnetic properties comparable to those of permanent magnets in use, is key for cost-effective technology. Towards this goal, we use a combined route of machine learning, based on experimental data, and first-principles calculations. While machine learning has been applied for the problem of rare-earth magnets [5], those studies have been based on the dataset created out of high-throughput calculations. Being dependent on calculation-based inputs, creation of such a database is not only computationally expensive, but also not devoid of approximations of the theory. Our study, on the other hand, is based on an exhaustive search of experimental data.

While a large volume of experimental data is available with numerical value of T_c , the corresponding dataset with the numerical values of M_s and K_u is small. On the other hand, there exists a sizable dataset with information of K_u being positive (easy axis) or negative (easy plane), and $\mu_0 M_s$ being larger or smaller than 1 T. We thus employ a regression model of machine-learning training to make predictions on numerical values of T_c , and a classification model to make predictions on sign of K_u , and $\mu_0 M_s$ being larger or smaller than 1 T. We apply the trained machine learning to 2:17 rare-earth transition-metal compounds with carbon and nitrogen in interstitials. We choose the compounds to contain abundant rare-earth Ce, and to be Fe rich to make them cost effective. Although the nitrogenated version of this series has been investigated [19], the systematic study of the carbonitride family is not available. The machine learning predicts T_c of the chosen carbonitride family to be larger than 600 K, $\mu_0 M_s > 1$ T, and $K_u > 0$, thereby indicating the possibility of them to become good solutions for cost-effective, permanent magnets. Subsequent first-principles calculations, show $T = 0$ K, $\mu_0 M_s$ to be larger than 1.65 T, and $K_u \gtrsim 1$ MJ/m³ for the entire family, Ce₂Fe_{17-x}Co_xCN ($x = 1, \dots, 7$). Calculated K_u values are found to be comparable to the state-of-the-art permanent magnet Nd₂Fe₁₄B for Ce₂Fe₁₅Co₂CN, Ce₂Fe₁₂Co₅CN, Ce₂Fe₁₁Co₆CN, and Ce₂Fe₁₀Co₇CN. This results in two figure of merits for hard magnets, $(BH)_{\max}$ and H_a in range of 444–540 kJ/m³ and approximately 1–14 T, respectively.

In spite of good magnetic properties, one of the limitations of practical applications of interstitial 2:17 magnets is the formation of nitrogen and carbon vacancies at high temperature. By calculating the N-(C)-vacancy formation energy, we show that carbonitrogenation codoping enhances the vacancy formation energy significantly, by 35–40% compared to the sum of individual doping. This is likely to improve the thermal stability at high-temperature condition.

Our computational exercise based on an exhaustive search of the experimental database, should motivate

future experimental processes in making high-performance 2:17 interstitial magnets, with the cheapest RE element Ce, the most abundant 3d metal, Fe and cheap nonmetal interstitial dopings like C and N. The estimated price-to-performance based on calculated energy product, and available market price [16] turns out to be 0.03–0.22 USD/J. The enhanced thermal stability of the carbonitride compounds against the vacancy formation of the light elements further boosts the promise of the suggested compounds.

ACKNOWLEDGMENT

The authors acknowledge support of DST Nano-mission for the computational facility used in this study.

APPENDIX

1. DFT details

DFT calculations for electronic structure, magnetocrystalline anisotropy are performed using the all-electron density-functional-theory code in full-potential linear-augmented-plane-wave (FP LAPW) basis, as implemented in the WIEN2K code [118]. For expensive structural optimization calculations, the plane-wave-based calculations, as implemented in the Vienna *ab initio* simulation package (VASP) [119], are carried out. The exchange-correlation functional is chosen to be the generalized-gradient approximation of Perdew, Burke, and Ernzerhof [120]. The localized nature of 4f states of Ce is captured through GGA+*U* calculations [121], with choice of $U = 6$ eV and $J_H = 0.8$ eV. For light rare earths like Ce the U value is shown to range from 4 to 7 eV, without affecting the physical properties much [108]. The spin-orbit coupling effect at Ce, and TM sites is captured through GGA+*U*+SOC calculations.

For FP LAPW calculations, APW + lo is used as the basis set, and the spherical harmonics are expanded upto $l = 10$ and the charge density and potentials are represented upto $l = 6$. The sphere radii are set at 2.5, 1.9, 2.34, 1.56, and 1.51 bohr for Ce, Fe, Co, N, and C. For good convergence, a RK_{max} value (the product of the smallest sphere radius and the largest plane-wave expansion wave vector) of 7.0 is used. We set the cutoff between core and valence states at -8.0 Ry. The k -space integrations are performed with 112 k points in irreducible Brillouin zone (BZ), following the report of use of 80 k points in irreducible BZ in the case of SmCo₅ to provide a good estimate of MAE [13]. Nevertheless, the convergence of results on k -space mesh is checked by carrying out calculation with 260 k points.

The structural optimization in plane-wave basis is carried out starting with the experimental structure of Sm₂Fe₁₇CN [107], replacing Sm with Ce, and relaxing all the internal coordinates until forces on all of the atoms become less than 0.001 eV/Å. Upon moving from Sm 2:17

carbide and nitride interstitial compounds to the Ce counterpart, the cell volume changes only nominally by 0.2% to 0.4% [6]. For the plane-wave calculations, energy cutoff of 600 eV and Monkhorst pack k -point mesh of $8 \times 8 \times 8$ are used.

All the calculations are performed by considering a collinear spin arrangement. The MAE is obtained by calculating the GGA+ U +SOC total energies of the system, in FP LAPW basis as $K_u = E_a - E_c$, where E_a and E_c are the energies for the magnetization oriented along the crystallographic a and c directions, respectively. For accurate estimates of vacancy formation energy, we also use FP LAPW basis.

2. Data preprocessing in machine learning

While constructing the database, we avoid inclusion of noisy data. We do bootstrapping to normalize the data, which is followed by removal of outliers with the help of violin plot. Data is removed if it lies outside of $Q1 - 1.5 \times IQR$ or $Q3 + 1.5 \times IQR$, where IQR is the interquartile range and Q1, Q2, and Q3 are lower, median and upper quartile, respectively. In the next step we identify correlated attributes using Pearson's correlation coefficient, which can be defined as

$$r = \frac{\sum_{i=1}^{i=n} (x_i - \bar{x})(y_i - \bar{y})}{\sqrt{\sum_{i=1}^{i=n} (x_i - \bar{x})^2} \sqrt{\sum_{i=1}^{i=n} (y_i - \bar{y})^2}}$$

Here n is the sample size, x_i and y_i are sample points and \bar{x} and \bar{y} are the sample means.

The heatmap obtained by using the above-mentioned correlation is shown in Fig. 9. The correlation between the attributes is mapped between 0 and 1, considering the absolute values. The highly correlated attributes with correlation greater than 0.75 are as follows.

1. Electronegativity difference between RE and TM ($\Delta\epsilon$) and CW average of atomic no. of TM ($\langle Z_{TM} \rangle$).
2. CW TM percentage (TM%) and CW average of atomic no. of TM ($\langle Z_{TM} \rangle$).
3. CW TM percentage (TM%) and electronegativity difference between RE and TM ($\Delta\epsilon$).
4. Total number of f electrons (f^n) and atomic no. of RE (Z_{RE}).
5. LE percentage (LE%) and CW average of atomic no. of TM ($\langle Z_{TM} \rangle$).
6. LE percentage (LE%) and electronegativity difference between RE and TM ($\Delta\epsilon$).
7. LE percentage (LE%) and CW TM percentage (TM%).

We thus discard $\Delta\epsilon$, LE%, Z_{RE} , and $\langle Z_{TM} \rangle$ from the list of attributes.

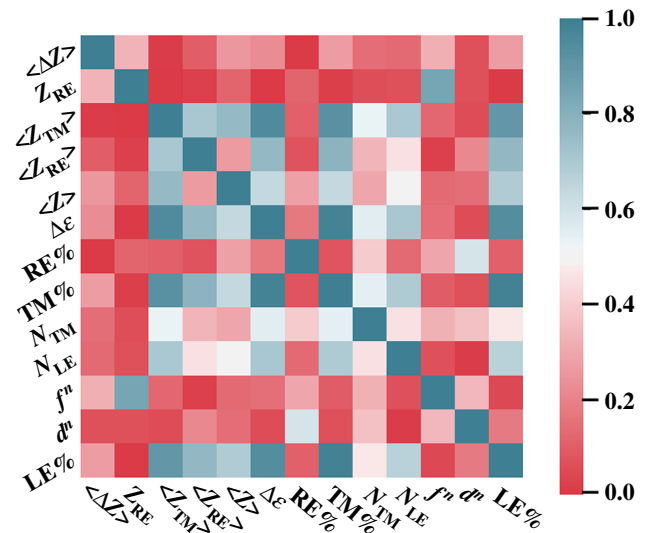


FIG. 9. Heatmap indicating the correlation between different attributes considered to build ML algorithm. The color code is shown in the side panel. The boxes with red represent weak or no correlation, whereas blue boxes represent strong correlation between the attributes.

3. Model construction for training in ML

The performance of a model can be quantified in terms of the coefficient of determination, which can be expressed as follows [122]:

$$R^2 = 1 - \frac{\sum_{i=1}^N [y_i - f(x_i)]^2}{\sum_{i=1}^N [y_i - \mu]^2}$$

for predictions $f(x_i)$ and a set of actual values y_i with mean μ . If the algorithm performs perfectly, R^2 score is 1. Figure 10 shows score R^2 for five different algorithms.

The RR algorithm circumvents issues in ordinary linear regression like overfitting or failure in finding a unique

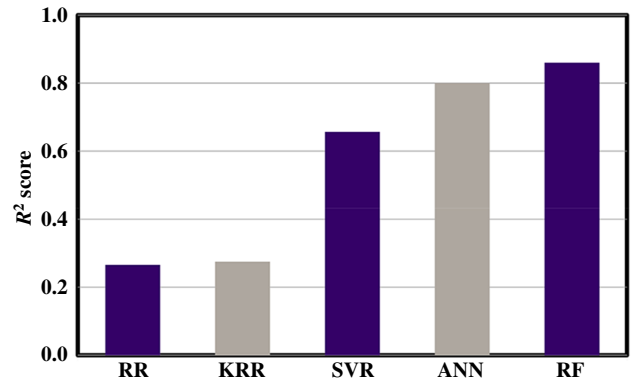


FIG. 10. Coefficient of determination R^2 score of five different ML algorithms applied to the T_c dataset.

solution due to multicollinearity. It develops on least-squares error by adding an extra penalty and regularization term to the loss function of ordinary linear regression. KRR builds on the ridge-regression technique by using a kernel trick [123] so that it can capture the nonlinearity present in the feature space. It can fit a nonlinear function by learning from a linear function spanned by a kernel, which in turn mimics a nonlinear function in the original space. SVR originated from support vector machines, which are mainly popular in the classification problem. It is based on the idea to search a hyperplane [124] by minimizing the error that is able to separate two different classes. SVR also uses the kernel trick to map the data into a high-dimensional feature space and then performs linear regression to fit the data. These three models are based on the same principle of linear regression and SVR is the best form according to our result. R^2 score is 0.66 for SVR whereas it is found to be poor (approximately 0.25) for the other two algorithms.

Apart from these we use two other algorithms, ANN and RF. The model performance scores are satisfactory for both of them. A simple ANN architecture called perceptron implements a processing element or artificial neuron called threshold logic unit (TLU), which can have one or more input(s) and one output. Each input is related to a weight. The TLU calculates the weighted sum of its inputs, applies a step function (generally Heaviside or sign function) to it and outputs the result. A perceptron [125] is simply a layer of TLUs operating in parallel and connected to all the

inputs. Training an ANN model is equivalent to learning each weight factor in an iterative cycle. A more complex system (multilayer perceptron) can be built by associating additional interconnected layers to the architecture. A well functioning system consists of an input layer, several hidden layers and an output layer. In our case we have one input layer, two hidden layers where rectified linear unit (ReLU) [126] is used as the activation function along with L2 regularization in the kernel, and an output layer. The constructed ANN model shows 0.80 as R^2 score.

Random forest is an ensemble method, which consists of multiple decision trees. Each tree is built on a portion of entire training data with a subset of the total number of attributes. The tree algorithm is based on a “top to bottom” approach, starting from a root node, it consists of many intermediate nodes and ends at leaf nodes. At each node of a tree a particular attribute classifies the data and helps to grow the tree. The prediction is based on accumulating the results from all such trees, taking ensemble average in the case of regression or considering votes from majority trees in the case of classification. Such an algorithm can capture the complex and nonlinear interaction between different attributes and can build a robust and sophisticated model. Our random forest consists of 100 trees built by bootstrapped [127] sampling of the training set. Each tree allows checking a maximum of \log_2 (number of features) while detecting the best split node. The quality of such a split is measured by using mean squared error (Gini

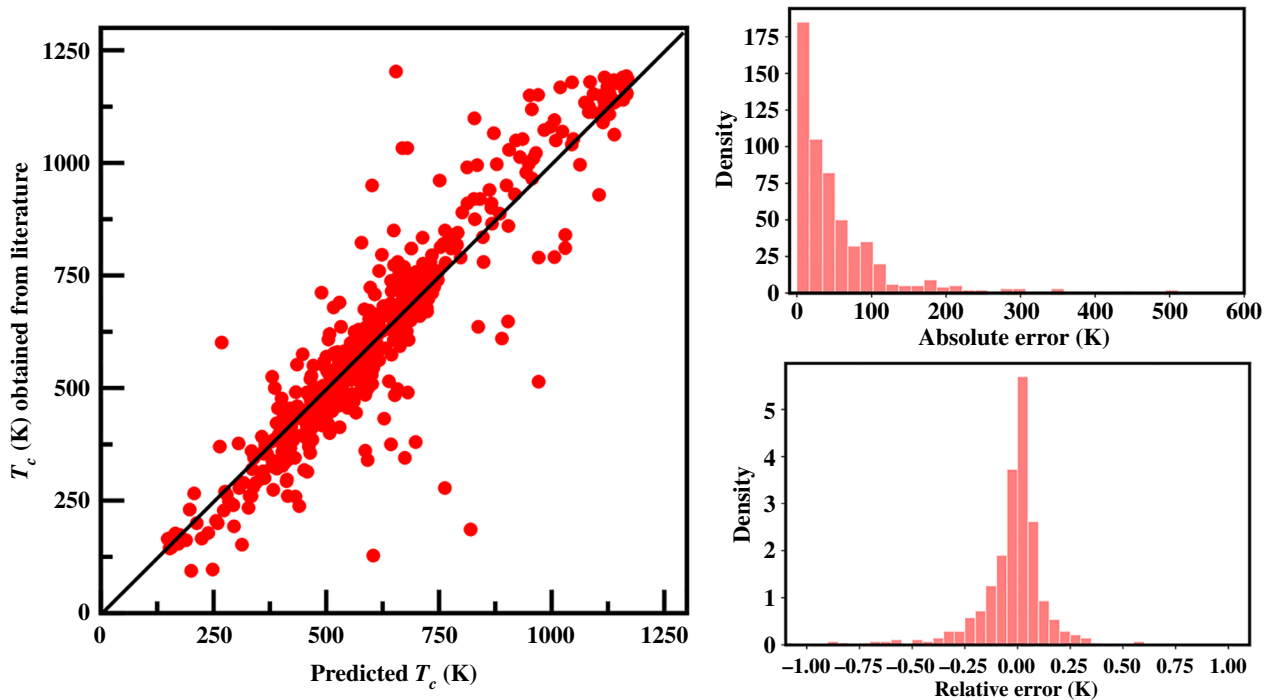


FIG. 11. Model output from rf algorithm for T_c of RETM intermetallics. The left panel shows the comparison of T_c obtained from the literature and predicted T_c . The distribution of absolute error between predicted T_c and actual T_c is shown in the upper, right panel, while the lower, right panel presents the distribution of relative error for the compounds with $T_c > 600$ K.

index) in regression (classification). The model efficiency is calculated by running out-of-bag samples down each of the trees. We use tenfold cross validation to extract the hyperparameter and to construct the best model.

Figure 11 shows the result of the best regression model using rf algorithm in the case of T_c . The plot in the left panel shows the predicted T_c versus T_c obtained from experiments. The determination score R^2 is high enough (0.86), indicating a good agreement between the predicted T_c and experimentally reported T_c . The mean absolute error in this model is 60 K. Additionally we evaluate absolute error and relative error for the compounds with $T_c > 600$ K (cf. Fig. 11, right panel). This analysis helps to determine the model performance for the compounds with $T_c > 600$ K as we are interested to predict RETM intermetallics with high T_c . The distribution of absolute error shows that for most of the compounds (approximately 85%) the absolute error is less than 100 K. For 65% of the predicted cases, the absolute error is less than 50 K. We also check the absolute error for the compounds with $T_c < 300$ K (not included in the figure). In this case our model predicts approximately 76% compounds with absolute error less than 100 K and 50% of instances are predicted with absolute error of 50 K. This observation prompts us to conclude that though the model prediction is in general good, it is less accurate for low T_c compounds compared to high T_c compounds. The distribution of relative error, expressed as $\epsilon_{\text{rel}} = (T_c^{\text{exp}} - T_c^{\text{predicted}})/T_c^{\text{exp}}$, provides further support to this statement, which is shown in the bottom, right panel of Fig. 11. The relative error distribution appears Gaussianlike with slight asymmetry about the mean position. The relative error is less in the right side of the mean position than the left side suggesting the

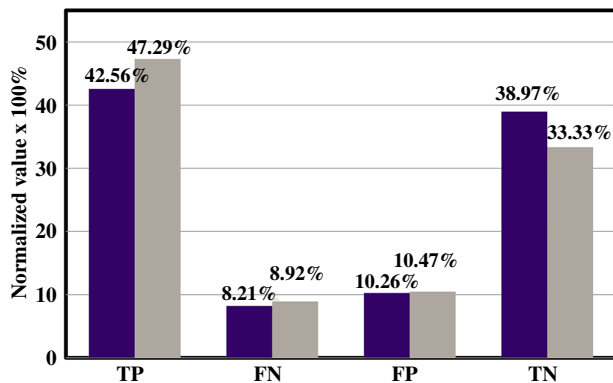


FIG. 12. Normalized confusion matrix for $\mu_0 M_s$ (violet) and K_u (gray) classification using tenfold cross validation. Here positive (negative) class represents either compounds with $\mu_0 M_s > (<) 1$ T, or compounds with uniaxial anisotropy, i.e., $K_u > (<) 0$ MJ/m³. True positive and negative or TP and TN are the compounds where their classes are predicted correctly. Whereas false positive (FP) and false negative (FN) are the off-diagonal terms of the matrix where the classes are incorrectly classified.

prediction of T_c suffers less overestimation than underestimation. As found, only 1% of the instances are having $\epsilon_{\text{rel}} > 50\%$, 3% of the instances have $50\% > \epsilon_{\text{rel}} > 30\%$, and 2% instances have $30\% > \epsilon_{\text{rel}} > 25\%$, most cases having tiny values of ϵ_{rel} . This gives us confidence in the accuracy of the predicted T_c for compounds with T_c s exceeding 600 K.

Turning to M_s , we use the random-forest algorithm to classify high M_s from low M_s compounds. The best model by performing tenfold cross validation is built up with 81.53% accuracy. The resultant confusion matrix is shown in Fig. 12. For classification problem, F1 score determines the balance between precision and recall. In this case F1 score 82.2% indicates good anticipation with slight favor towards the prediction of compounds with high M_s ($\mu_0 M_s > 1$) (83.8%) compared to the compounds with low M_s ($\mu_0 M_s < 1$) (79.2%).

Similar to M_s , we use the random-forest algorithm for K_u , to classify positive K_u from negative K_u compounds. The best model by performing tenfold cross validation, in this case, is built up with 80.62% accuracy like M_s , in this case F1 score for positive K_u is 83% and for negative is K_u 77.5% suggesting slight preference of classification towards positive K_u , which is also captured in the plot of the confusion matrix as shown in Fig. 12.

- [1] K. Buschow, New developments in hard magnetic materials, *Rep. Prog. Phys.* **54**, 1123 (1991).
- [2] J. M. D. Coey, Hard magnetic materials: A perspective, *IEEE Trans. Magn.* **47**, 4671 (2011).
- [3] Hong Sun, Y. Otani, and J. M. D. Coey, Gas-phase carbonation of $R_2\text{Fe}_{17}$, *J. Magn. Magn. Mater.* **104–107**, 1439 (1992).
- [4] A. Vishina, O. Y. Vekilova, T. Björkman, A. Bergman, H. C. Herper, and O. Eriksson, High-throughput and data-mining approach to predict new rare-earth free permanent magnets, *Phys. Rev. B* **101**, 094407 (2020).
- [5] J. J. Möller, W. Körner, G. Krugel, D. F. Urban, and Christian Elsässer, Compositional optimization of hard-magnetic phases with machine-learning models, *Acta Mater.* **153**, 53 (2018).
- [6] T. Pandey, M.-H. Du, and D. S. Parker, Tuning the Magnetic Properties and Structural Stabilities of the 2-17-3 Magnets $\text{Sm}_2\text{Fe}_{17}\text{X}_3$ ($X = \text{C}, \text{N}$) by Substituting La or Ce for Sm, *Phys. Rev. Appl.* **9**, 034002 (2018).
- [7] L. Ke and D. D. Johnson, Intrinsic magnetic properties in $\text{R}(\text{Fe}_{1-x}\text{Co}_x)_{11}\text{TiZ}$ ($R = \text{Y}$ and Ce ; $Z = \text{H}, \text{C}$, and N), *Phys. Rev. B* **94**, 024423 (2016).
- [8] J. M. D. Coey, Permanent magnets: Plugging the gap, *Scr. Mater.* **67**, 524 (2012).
- [9] S. V. Halilov, H. Eschrig, A. Y. Perlov, and P. M. Oppeneer, Adiabatic spin dynamics from spin-density-functional theory: Application to Fe, Co, and Ni, *Phys. Rev. B* **58**, 293 (1998).
- [10] A. Georges, G. Kotliar, W. Krauth, and M. J. Rozenberg, Dynamical mean-field theory of strongly correlated

- fermion systems and the limit of infinite dimensions, *Rev. Mod. Phys.* **68**, 13 (1996).
- [11] W. Körner, G. Krugel, and C. Elsässer, Theoretical screening of intermetallic ThMn₁₂-type phases for new hard-magnetic compounds with low rare earth content, *Sci. Rep.* **6**, 24686 (2016).
- [12] H. Brooks, Ferromagnetic anisotropy and the itinerant electron model, *Phys. Rev.* **58**, 909 (1940).
- [13] P. Larson, I. I. Mazin, and D. A. Papaconstantopoulos, Calculation of magnetic anisotropy energy in SmCo₅, *Phys. Rev. B* **67**, 214405 (2003).
- [14] S. Yehia, S. H. Aly, and A. E. Aly, Electronic band structure and spin-density maps of SmCo₅, *Comput. Mater. Sci.* **41**, 482 (2008).
- [15] H. Ucar, R. Choudhary, and D. Paudyal, An overview of the first principles studies of doped RE – TM₅ systems for the development of hard magnetic properties, *J. Magn. Magn. Mater.* **496**, 165902 (2020).
- [16] J. M. D. Coey, Perspective and prospects for rare earth permanent magnets, *Engineering* **6**, 119 (2020).
- [17] D. Odkhuu and S. C. Hong, First-Principles Prediction of Possible Rare-Earth Free Permanent Magnet of Tetragonal FeCo with Enhanced Magnetic Anisotropy and Energy Product through Interstitial Nitrogen, *Phys. Rev. Appl.* **11**, 054085 (2019).
- [18] D. Odkhuu, T. Ochirkhuyag, and S. C. Hong, Enhancing Energy Product and Thermal Stability of SmFe₁₂ by Interstitial Doping, *Phys. Rev. Appl.* **13**, 054076 (2020).
- [19] Xie Xu and S. A. Shaheen, Structural and magnetic properties of rare-earth iron nitride Ce₂(Fe_{1-x}Co_x)₁₇N_y series, *J. Appl. Phys.* **73**, 5896 (1993).
- [20] H. Fujii and H. Sun, in *Handbook of Magnetic Materials* (Elsevier, Amsterdam, 1995), p. 303.
- [21] X. Chen, Z. Altounian, and D. H. Ryan, Carbonitrides of R₂Fe₁₇ prepared by gas-solid reaction, *J. Magn. Magn. Mater.* **125**, 169 (1993).
- [22] <https://icsd.nist.gov/guide.html>.
- [23] K. H. J. Buschow, *Handbook of Magnetic Materials* (Elsevier, Amsterdam, 1991–1995), Vol. 6 & 9.
- [24] J. M. D. Coey, *Magnetism and Magnetic Materials* (Cambridge University Press, Cambridge, 2010).
- [25] Shiqiang Liu, Sm–Co high-temperature permanent magnet materials, *Chin. Phys. B* **28**, 017501 (2019).
- [26] S. R. Mishra, Gary J. Long, O. A. Pringle, D. P. Middleton, Z. Hu, W. B. Yelon, F. Grandjean, and K. H. J. Buschow, A magnetic neutron diffraction, and Mössbauer spectral study of the Ce₂Fe_{17-x}Al_x solid solutions, *J. Appl. Phys.* **79**, 3145 (1996).
- [27] H. Klesnar, K. Hiebl, and P. Rogl, Magnetic behaviour of RE₂Ti₁₅Ga₂; RE ≡ mischmetal MM, Y, Ce, Pr, Nd, Sm; T ≡ Fe, Co and RE₂Fe_{15-x}Co_xGa₂; RE ≡ Y, Nd, *J. Less-Common Metals* **154**, 217 (1989).
- [28] R. Guetari, R. Bez, A. Belhadj, K. Zehani, A. Bezergheanu, N. Mliki, L. Bessais, and C. B. Cizmas, Influence of Al substitution on magnetocaloric effect of Pr₂Fe_{17-x}Al_x, *J. Alloys Compd.* **588**, 64 (2014).
- [29] Y. Otani, D. P. F. Hurley, Hong Sun, and J. M. D. Coey, Magnetic properties of a new family of ternary rare-earth iron nitrides R₂Fe₁₇N_{3-δ}, *J. Appl. Phys.* **69**, 5584 (1991).
- [30] M. Merches, W. E. Wallace, and R. S. Craig, Magnetic and structural characteristics of some 2:17 rare earth-cobalt systems, *J. Magn. Magn. Mater.* **24**, 97 (1981).
- [31] F. Pourarian, R. Obermyer, Y. Zheng, S. G. Sankar, and W. E. Wallace, Crystal structure and magnetic characteristics of alloys based on R - Fe - Si (R = Y, Nd, Gd, Dy, Ho, Er), *J. Appl. Phys.* **73**, 6272 (1993).
- [32] F. Weitzer, H. Klesnar, K. Hiebl, and P. Rogl, Magnetism of Pr₂(Fe_{1-x-y}Co_xAl_y)₁₇ alloys with a Th₂Zn₁₇-type structure, *J. Appl. Phys.* **67**, 2544 (1990).
- [33] X. P. Zhong, R. J. Radwanski, F. R. de Boer, T. H. Jacobs, and K. H. J. Buschow, Magnetic and crystallographic characteristics of rare-earth ternary carbides derived from R₂Fe₁₇ compounds, *J. Magn. Magn. Mater.* **86**, 333 (1990).
- [34] A. T. Pedziwiatr and W. E. Wallace, Magnetism of R₂Co_{14-x}Si_xB systems (R = Y, Pr, and Nd), *J. Appl. Phys.* **61**, 3439 (1987).
- [35] R. van Mens, Ternary phase studies of Nd - Fe - X where X = C, Si, Pb, Sn, *J. Magn. Magn. Mater.* **61**, 24 (1986).
- [36] Hu Bo-Ping and J. M. D. Coey, Effect of hydrogen on the curie temperature of Nd₂(Fe₁₅M₂); M ≡ Ai, Si, Co, *J. Less-Common Metals* **142**, 295 (1988).
- [37] H. Y. Chen, S. G. Sankar, and W. E. Wallace, Spin reorientation in substituted Nd₂Co₁₇ compounds, *J. Appl. Phys.* **63**, 3969 (1988).
- [38] M. Juczyk and W. E. Wallace, Magnetic behavior of R_{1.9}Zr_{0.1}Fe₁₄B and R_{1.9}Zr_{0.1}Fe₁₂Co₂B compounds, *J. Magn. Magn. Mater.* **59**, L182 (1986).
- [39] Y. G. Xiao, G. H. Rao, Q. Zhang, G. Y. Liu, Y. Zhang, and J. K. Liang, Crystallographic and magnetic studies on iron-rich mixed rare-earth intermetallics (Nd/Tb)₂(Fe/Al)₁₇, *J. Alloys Compd.* **407**, 1 (2006).
- [40] E. Girt, M. Guillot, I. P. Swainson, Kannan M. Krishnan, Z. Altounian, and G. Thomas, Structural and magnetic properties of Nd₂Fe_{17-δ}Ga_δ (δ ≤ 2), *J. Appl. Phys.* **87**, 5323 (2000).
- [41] Wolfgang Körner, Georg Krugel, and Christian Elsässer, Theoretical screening of intermetallic ThMn₁₂ -type phases for new hard-magnetic compounds with low rare earth content, *Sci. Rep.* **6**, 24686 (2016).
- [42] A. M. Schönhöbel, R. Madugundo, O. Yu. Vekilova, O. Eriksson, H. C. Herper, J. M. Barandiaran, and G. C. Hadjipanayis, Intrinsic magnetic properties of SmFe_{12-x}V_x alloys with reduced V-concentration, *J. Alloys Compd.* **786**, 969 (2019).
- [43] Y. Z. Wang, G. C. Hadjipanayis, A. Kim, D. J. Sellmyer, and W. B. Yelon, Structure and magnetic properties of RFe₁₀V₂N_x compounds, *J. Magn. Magn. Mater.* **104–107**, 1132 (1992).
- [44] E. P. Wohlfarth and K. H. J. Buschow, *Handbook of Magnetic Materials* (Elsevier, Amsterdam, 1988), Vol. 4.
- [45] Y. Z. Wang, B. P. Hu, X. L. Rao, G. C. Liu, L. Yin, W. Y. Lai, W. Gong, and G. C. Hadjipanayis, Structural and magnetic properties of NdFe_{12-x}Mo_xN_{1-δ} compounds, *J. Appl. Phys.* **73**, 6251 (1993).
- [46] D. P. F. Hurley and J. M. D. Coey, Gas-phase interstitially modified intermetallics R(Fe₁₁Ti)Z_{1-δ}: I. Magnetic properties of the series R(Fe₁₁Ti)C_{1-δ}: R = Y, Nd, Sm, Gd,

- Tb, Dy, Ho, Er, Tm, Lu, *J. Phys. Condens. Matter* **4**, 5573 (1992).
- [47] Yosuke Harashima, Kiyoyuki Terakura, Hiori Kino, Shoji Ishibashi, and Takashi Miyake, Nitrogen as the best interstitial dopant among $X = B, C, N, O,$ and F for strong permanent magnet $NdFe_{11}TiX$: First-principles study, *Phys. Rev. B* **92**, 184426 (2015).
- [48] Y. G. Xiao, G. H. Rao, Q. Zhang, J. Luo, G. Y. Liu, Y. Zhang, and J. K. Liang, Formation, structure and magnetic properties of $TbFe_{12-x}Mo_x$ ($x = 0.5-3.0$) compounds, *Phys. B* **369**, 56 (2005).
- [49] V. K. Sinha, S. F. Cheng, W. E. Wallace, and S. G. Sankar, Magnetic behavior of heavy rare earth $RTiFe_{11-x}Co_x$ alloys, *J. Magn. Magn. Mater.* **81**, 227 (1989).
- [50] M. Jurczyk, Magnetic properties of $RFe_{10.8}Re_{1.2}$ compounds ($R = Y, Tb$ and Ho), *J. Magn. Magn. Mater.* **89**, L5 (1990).
- [51] M. Katter, J. Wecker, C. Kuhrt, L. Schultz, X. C. Kou, and R. Grössinger, Structural and intrinsic magnetic properties of $(Sm_{1-x}Nd_x)_2Fe_{17}N_{\approx 2.7}$ and $(Sm_{1-x}Nd_x)_2(Fe_{1-z}Co_z)_{17}N_{\approx 2.7}$, *J. Magn. Magn. Mater.* **111**, 293 (1992).
- [52] M. Jurczyk and W. E. Wallace, Magnetic behavior of $R_{1.9}Zr_{0.1}Fe_{14}B$ and $R_{1.9}Zr_{0.1}Fe_{12}Co_2B$ compounds, *J. Magn. Magn. Mater.* **59**, L182 (1986).
- [53] Yang Fu-ming, Li Qing-an, Zhao Ru-wen, Kuang Jian-ping, F. R. de Boer, J. P. Liu, K. V. Rao, G. Nicolaides, and K. H. J. Buschow, Magnetic behaviour of heavy rare earth compounds of the type $RFe_{10}Cr_2$, *J. Alloys Compd.* **177**, 93 (1991).
- [54] Bao-gen Shen, Fang-wei Wang, Lin-shu Kong, Lei Cao, and Hui-qun Guo, Formation and magnetic properties of $R_2Fe_{17-x}Ga_xC_2$ compounds prepared by arc-melting, *J. Magn. Magn. Mater.* **127**, L267 (1993).
- [55] X. C. Kou, T. S. Zhao, R. Grössinger, and F. R. de Boer, Ac-susceptibility anomaly and magnetic anisotropy of R_2Co_{17} compounds, with $R = Y, Ce, Pr, Nd, Sm, Gd, Tb, Dy, Ho, Er, Tm,$ and Lu , *Phys. Rev. B* **46**, 6225 (1992).
- [56] Zhi-gang Sun, Shao-ying Zhang, Hong-wei Zhang, Jing-yun Wang, and Bao-gen Shen, The effect of manganese substitution on the magnetic properties of Ce_2Co_{17} compounds, *J. Phys. Condens. Matter* **12**, 2495 (2000).
- [57] Z. X. Tang, E. W. Singleton, and G. C. Hadjipanayis, Rare – earth transition metal carbides, *IEEE Trans. Magn.* **28**, 2572 (1992).
- [58] C. H. de Groot, K. H. J. Buschow, and F. R. de Boer, Magnetic properties of $R_2Co_{17-x}Al_x$ compounds ($R = Ho, Dy, Y$), *Phys. B* **229**, 213 (1997).
- [59] L. Zhang, D. C. Zeng, Y. N. Liang, J. C. P. Klaasse, E. Bruck, Z. Y. Liu, F. R. de Boer, and K. H. J. Buschow, Magnetic properties of $Er_2Co_{17-x}Si_x$ compounds, *J. Magn. Magn. Mater.* **214**, 31 (2000).
- [60] Bing Liang, Bao-gen Shen, Fang-wei Wang, Tong-yun Zhao, Zhao-hua Cheng, Shao-ying Zhang, Hua-yang Gong, and Wen-shan Zhan, The magnetic properties of $Gd_2Co_{17-x}Ga_x$ compounds, *J. Appl. Phys.* **82**, 3452 (1997).
- [61] Zhi-gang Sun, Shao-ying Zhang, Hong-wei Zhang, and Bao-gen Shen, The structure and magnetic properties of $Gd_2Co_{17-x}Mn_x$ ($x = 0-4$) compounds, *J. Alloys Compd.* **322**, 69 (2001).
- [62] Lin Qin, Sun Yunxi, Lan Jian, Lu Shizhong, and Jiang Hongwei, Crystallographic and magnetic properties of $R_2Fe_{17}C_x$ with $R = Y, Pr, Nd, Sm, Gd, Dy,$ and Er , *Chinese Phys. Lett.* **8**, 267 (1991).
- [63] Jing-Yun Wang, Bao-Gen Shen, Shao-Ying Zhang, Wen-Shan Zhan, and Li-Gang Zhang, Structure, exchange interactions and magnetic anisotropy of $Ho_2Co_{17-x}Si_x$ compounds, *J. Appl. Phys.* **87**, 427 (2000).
- [64] O. Isnard and M. Guillot, Investigation of the magnetic properties of Nd_2Fe_{17} and $Nd_2Fe_{17}H_x$ ($x = 3, 4, 9$) in high magnetic field, *J. Appl. Phys.* **87**, 5326 (2000).
- [65] Zhi-gang Sun, Hong-wei Zhang, Shao-ying Zhang, and Bao-gen Shen, Structure and magnetic properties of $Nd_2(Co, Mn)_{17}$ compounds, *Phys. B* **305**, 127 (2001).
- [66] M. V. Satyanarayana, H. Fujii, and W. E. Wallace, Magnetic and structural investigations on substituted $Pr_2Co_{17-x}T_x$ systems ($T = Fe, Mn, Cr, Cu$ and Al), *J. Magn. Magn. Mater.* **40**, 241 (1984).
- [67] Zhi-gang Sun, Hong-wei Zhang, Shao-ying Zhang, Jing-yun Wang, and Bao-gen Shen, Structure and magnetic properties of $Sm_2Fe_{17-x}Mn_x$ compounds, *J. Phys. D: Appl. Phys.* **33**, 485 (2000).
- [68] Zhi-gang Sun, Hong-wei Zhang, Shao-ying Zhang, Jing-yun Wang, and Bao-gen Shen, Structure and magnetic properties of $Tb_2Co_{17-x}Mn_x$ compounds, *J. Appl. Phys.* **87**, 8666 (2000).
- [69] E. A. Tereshina, H. Drulis, Y. Skourski, and I. S. Tereshina, Strong room-temperature easy-axis anisotropy in $Tb_2Fe_{17}H_3$: An exception among R_2Fe_{17} hydrides, *Phys. Rev. B* **87**, 214425 (2013).
- [70] Yingchang Yang, Qi Pan, Xiaodong Zhang, and Senlin Ge, Magnetic properties of $R_2Fe_{17}CN_x$, *J. Appl. Phys.* **72**, 2989 (1992).
- [71] Z. Altounian, Xu Bo Liu, and Er Girt, Formation, structure and hard magnetic properties of $Sm_2Fe_{17-x}Co_xC_y$ compounds, *J. Phys. Condens. Matter* **15**, 3315 (2003).
- [72] Linshu Kong, Jiabin Yao, Minghou Zhang, and Yingchang Yang, Magnetic properties of $Sm_2(Fe_{1-x}Co_x)_{17}C$ and $Y_2(Fe_{1-x}Co_x)_{17}C$, *J. Appl. Phys.* **70**, 6154 (1991).
- [73] O. Isnard, S. Miraglia, J. L. Soubeyroux, D. Fruchart, and P. L’Heritier, A structural analysis and some magnetic properties of the $R_2Fe_{17}H_x$ series, *J. Magn. Magn. Mater.* **137**, 151 (1994).
- [74] D. P. Middleton, S. R. Mishra, Gary J. Long, O. A. Pringle, Z. Hu, W. B. Yelon, F. Grandjean, and K. H. J. Buschow, A magnetic, neutron-diffraction, and Mössbauer spectral study of the $Ce_2Fe_{17-x}Si_x$ solid solutions, *J. Appl. Phys.* **78**, 5568 (1995).
- [75] T. Pandey and David S. Parker, Magnetic properties and magnetocrystalline anisotropy of Nd_2Fe_{17} , $Nd_2Fe_{17}X_3$, and related compounds, *Sci. Rep.* **8**, 3601 (2018).
- [76] H. Luo, Z. Hu, W. B. Yelon, S. R. Mishra, G. J. Long, O. A. Pringle, D. P. Middleton, and K. H. J. Buschow, Neutron diffraction structural study of $Ce_2Fe_{17-x}Ga_x$, *J. Appl. Phys.* **79**, 6318 (1996).
- [77] O. Isnard, S. Miraglia, D. Fruchart, j. Deportes, and P. L’Heritier, Magnetic properties of fully nitrogenated,

- $R_2\text{Fe}_{17}\text{N}_3$ ($R = \text{Ce}, \text{Nd}, \text{Pr}$), *J. Magn. Magn. Mater.* **131**, 76 (1994).
- [78] A. V. Andreev, D. Rafaja, J. Kamarad, Z. Arnold, Y. Homma, and Y. Shiokawa, Magnetic properties of the $\text{Lu}_2\text{Fe}_{17-x}\text{Si}_x$ single crystals, *J. Alloys Compd.* **383**, 40 (2004).
- [79] See Supplemental Material at <http://link.aps.org/supplemental/10.1103/PhysRevApplied.14.034024> for the datasets for T_c , $\mu_0 M_s$, and K_u .
- [80] V. Psycharis, M. Anagnostou, C. Christides, and D. Niarchos, Rietveld analysis of x-ray powder diffraction patterns for the new $\text{SmFe}_{10}\text{Mo}_2\text{N}_x$ nitride compound, *J. Appl. Phys.* **70**, 6122 (1991).
- [81] K. Ohashi, Y. Tawara, R. Osugi, and M. Shimao, Magnetic properties of Fe-rich rare-earth intermetallic compounds with a ThMn_{12} structure, *J. Appl. Phys.* **64**, 5714 (1988).
- [82] Satoshi Hirose, Yutaka Matsuura, Hitoshi Yamamoto, Setsuo Fujimura, and Masato Sagawa, Magnetization and magnetic anisotropy of $\text{R}_2\text{Fe}_{14}\text{B}$ measured on single crystals, *J. Appl. Phys.* **59**, 873 (1986).
- [83] C. Abache and H. Oesterreicher, Magnetic properties of compounds $\text{R}_2\text{Fe}_{14}\text{B}$, *J. Appl. Phys.* **57**, 4112 (1985).
- [84] Z. X. Tang, G. C. Hadjipanayis, and V. Papaefthymiou, Intrinsic and hard magnetic properties of rapidly quenched $\text{NdFe}_{10}\text{Mo}_2\text{N}_x$ ribbons, *J. Alloys Compd.* **194**, 87 (1993).
- [85] Y. Z. Wang, B. P. Hu, X. L. Rao, G. C. Liu, L. Yin, W. Y. Lai, W. Gong, and G. C. Hadjipanayis, Structural and magnetic properties of $\text{NdFe}_{12-x}\text{Mo}_x\text{N}_{1-\delta}$ compounds, *J. Appl. Phys.* **73**, 6251 (1993).
- [86] M. Anagnostou, C. Christides, and D. Niarchos, Nitrogenation of the $\text{RFe}_{10}\text{Mo}_2$ ($R = \text{rare earth}$) compounds with ThMn_{12} type structure, *Solid State Commun.* **78**, 681 (1991).
- [87] Y. Zhang and C. Ling, A strategy to apply machine learning to small datasets in materials science, *npj Comput. Mater.* **4**, 25 (2018).
- [88] Anita Halder, Aishwaryo Ghosh, and Tanusri Saha Dasgupta, Machine-learning-assisted prediction of magnetic double perovskites, *Phys. Rev. Mater.* **3**, 084418 (2019).
- [89] L. Ward, A. Agrawal, A. Choudhary, and C. Wolverton, A general-purpose machine learning framework for predicting properties of inorganic materials, *npj Comp. Mat.* **2**, 16028 (2016).
- [90] Wessel N. van Wieringen, Lecture notes on ridge regression, arXiv:1509.09169v5 (2020).
- [91] Vladimir Vovk, in *Empirical Inference* (Springer, Berlin, Heidelberg, 2013), ISBN 9783642411366.
- [92] Leo Breiman, Random forests, *Mach. Learn.* **45**, 5 (2001).
- [93] Andy Liaw and Matthew Wiener, Classification and regression by randomForest, *R News* **2**, 18 (2002).
- [94] Harris Drucker, C. J. C. Burges, Linda Kaufman, Alex J. Smola, and Vladimir Vapnik, *Support Vector Regression Machines*, Proceedings of the International Conference on Advances in Neural Information Processing Systems, Denver, CO, USA, 1996, edited by Michael Mozer, Michael I. Jordan, Thomas Petsche (MIT Press, 1997), p. 155.
- [95] Mohamad Hassoun, *Fundamentals of Artificial Neural Networks* (MIT Press, Cambridge, 1995).
- [96] Anton O. Oliynyk, Erin Antono, Taylor D. Sparks, Leila Ghadbeigi, Michael W. Gaultois, Bryce Meredig, and Arthur Mar, High-throughput machine-learning-driven synthesis of full-heusler compounds, *Chem. Mater.* **28**, 7324 (2016).
- [97] Fleur Legrain, Jesús Carrete, Ambroise van Roekeghem, Georg K. H. Madsen, and Natalio Mingo, Materials screening for the discovery of new half-heuslers: Machine learning versus ab initio methods, *J. Phys. Chem. B* **122**, 625 (2018).
- [98] Jesús Carrete, Wu Li, Natalio Mingo, Shidong Wang, and Stefano Curtarolo, Finding Unprecedentedly Low-Thermal-Conductivity Half-Heusler Semiconductors via High-Throughput Materials Modeling, *Phys. Rev. X* **4**, 011019 (2014).
- [99] D. Andrew Carr, Mohammed Lach-hab, Shujing Yang, Iosif I. Vaisman, and Estela Blaisten-Barojas, Machine learning approach for structure-based zeolite classification, *Microporous Mesoporous Mater.* **117**, 339 (2009).
- [100] H. Fujii, K. Tatami, M. Akayama, and K. Yamamoto, in *Proc. 6th Int. Conf. on Ferrites, ICF6, Tokyo and Kyoto, Japan* (The Japan Society of Powder and Powder Metallurgy, Tokyo, 1992), p. 1081.
- [101] H. Fujii, M. Akayama, K. Nakao, and K. Tatami, Effect of interstitial hydrogen and nitrogen on magnetic and structural properties of R_2T_{17} ($R = \text{Y}, \text{Ce}$ and Sm ; $T = \text{Fe}, \text{Co}$ and Ni), *J. Alloys Compd.* **219**, 10 (1995).
- [102] Z. Altounian, X. Chen, L. X. Liao, D. H. Ryan, and J. O. Ström-Olsen, Structure and magnetic properties of rare-earth iron nitrides, carbides and carbonitrides, *J. Appl. Phys.* **73**, 6017 (1993).
- [103] X. Chen, Z. Altounian, and D. H. Ryan, Carbonitrides of R_2Fe_{17} prepared by gas-solid reaction, *J. Magn. Magn. Mater.* **125**, 169 (1993).
- [104] K. H. J. Buschow, T. H. Jacobs, and W. Coene, Structure and properties of novel ternary Fe-rich rare earth-carbides, *IEEE Trans. Magn.* **MAG-26**, 1364 (1990).
- [105] J. P. Liu, K. Bakker, E. R. de Boer, T. H. Jacobs, D. B. de Mooij, and K. H. J. Buschow, Magnetic properties of $\text{R}_2\text{Fe}_{17}\text{N}_{2.7}$ compounds, *J. Less-Common Met.* **170**, 109 (1991).
- [106] W. G. Haije, T. H. Jacobs, and K. H. J. Buschow, Magnetic structure of ternary rare earth carbides of the type $\text{R}_2\text{Fe}_{17}\text{C}$, *J. Less-Common Met.* **163**, 353 (1990); T. W. Capehart, R. K. Misra, and F. E. Pickerton, $\text{Sm}_2\text{Fe}_{17}\text{N}_x$: Site and valence of the interstitial nitrogen, *App. Phys. Lett.* **58**, 1395 (1991).
- [107] X. C. Kou, R. Grossinger, M. Katter, J. Wecker, L. Schultz, T. H. Jacobs, and K. H. J. Buschow, Intrinsic magnetic properties of $\text{R}_2\text{Fe}_{17}\text{C}_y\text{N}_x$ compounds: ($R = \text{Y}, \text{Sm}, \text{Er}$, and Tm), *J. Appl. Phys.* **70**, 2272 (1991).
- [108] I. L. M. Locht, Y. O. Kvashnin, D. C. M. Rodrigues, M. Pereiro, A. Bergman, L. Bergqvist, A. I. Lichtenstein, M. I. Katsnelson, A. Delin, A. B. Klautau, B. Johansson, I. Di Marco, and O. Eriksson, Standard model of the rare earths analyzed from the Hubbard I approximation, *Phys. Rev. B* **94**, 085137 (2016).
- [109] R. K. Chouhan, A. K. Pathak, D. Paudyal, and V. K. Pecharsky, High performance magnetic material with Ce

- and La: An alternative to Nd-Fe-B magnet, SmCo-a case of strong J-mixing, arXiv:806.01990.
- [110] B. Szpunar, Magnetic anisotropy of SmCo-a case of strong J-mixing, *Acta Phys. Pol. A* **60**, 791 (1981); T. S. Zhao, H.-M. Jin, R. Grossinger, X.-C. Kou, and H. R. Kirchmayr, Analysis of the magnetic anisotropy in SmCo₅ and GdCo₅, *J. Appl. Phys.* **70**, 6134 (1991); I. A. Al-Omari, R. Skomski, R. A. Thomas, D. Leslie-Pelecky, and D. J. Sellmyer, High-temperature magnetic properties of mechanically alloyed SmCo₅ and YCo₅ magnets, *IEEE Trans. Magn.* **MAG-37**, 2534 (2001).
- [111] N. Thuy, J. Franse, N. Hong, and T. Hien, 3D anisotropy in R-3D intermetallics, *J. Phys. Colloques* **49**, 499 (1988).
- [112] P. Bruno, Tight-binding approach to the orbital magnetic moment and magnetocrystalline anisotropy of transition-metal monolayers, *Phys. Rev. B* **39**, 865 (1989).
- [113] J. Herbst, R₂Fe₁₄B materials: Intrinsic properties and technological aspects, *Rev. Mod. Phys.* **63**, 819 (1991).
- [114] T. Miyake and H. Akai, Quantum theory of rare-earth magnets, *J. Phys. Soc. Jpn* **87**, 041009 (2018).
- [115] Y. Hirayama, Y. Takahashi, S. Hirose, and K. Hono, NdFe₁₂N_x hard-magnetic compound with high magnetization and anisotropy field, *Scr. Mater.* **95**, 70 (2015).
- [116] K. H. J. Buschow, *Concise Encyclopedia of Magnetic and Superconducting Materials* (Elsevier, Amsterdam, 2005).
- [117] J. M. D. Coey, *Magnetism and Magnetic Materials* (Cambridge University Press, Cambridge, 2010).
- [118] P. Blaha, K. Schwarz, G. K. H. Madsen, D. Kvasnicka, and J. Luitz, *WIEN2K, An Augmented Plane Wave + Local Orbitals Program for Calculating Crystal Properties* (Technische Universität Wien, Vienna, 2001).
- [119] G. Kresse and J. Hafner, Ab initio molecular dynamics for liquid metals, *Phys. Rev. B* **47**, R558 (1993); G. Kresse and J. Furthmüller, Efficient iterative schemes for ab initio total-energy calculations using a plane-wave basis set, *Phys. Rev. B* **54**, 11169 (1996).
- [120] J. P. Perdew, K. Burke, and M. Ernzerhof, Generalized Gradient Approximation Made Simple, *Phys. Rev. Lett.* **77**, 3865 (1996); **78**, 1396(E) (1997).
- [121] A. I. Liechtenstein, V. I. Anisimov, and J. Zaanen, Density-functional theory and strong interactions: Orbital ordering in Mott-Hubbard insulators, *Phys. Rev. B* **52**, R5467 (1995).
- [122] Nico J. D. Nagelkerke, A note on a general definition of the coefficient of determination, *Biometrika* **78**, 691 (1991).
- [123] Bernhard Schölkopf, *The Kernel Trick for Distances, Advances in Neural Information Processing Systems* (MIT Press, Cambridge, 2001), p. 301.
- [124] Support Vector Regression(SVR), http://lisa.epfl.ch/teaching/lectures/ML_PhD/Notes/nu-SVM-SVR.pdf.
- [125] I. Stephen, Perceptron-based learning algorithms, *IEEE Trans. Neural Netw.* **50**, 179 (1990).
- [126] Di Wei, Anurag Bhardwaj, and Jianing Wei, *Deep Learning Essentials* (Packt Publishing, Birmingham, 2018).
- [127] Bradley Efron and Robert J. Tibshirani, *An Introduction to the Bootstrap* (CRC Press, Washington, D.C, 1994).